J Oceanogr (2012) 68:21–43
DOI 10.1007/s10872-011-0083-7

SPECIAL SECTION: REVIEW

New developments in mode-water research: Dynamic and climatic effects

Review on North Pacific Subtropical Countercurrents and Subtropical Fronts: role of mode waters in ocean circulation and climate

Fumiaki Kobashi · Atsushi Kubokawa

Received: 13 March 2011 / Revised: 8 September 2011 / Accepted: 9 September 2011 / Published online: 25 November 2011
© The Oceanographic Society of Japan and Springer 2011

Abstract A Subtropical Countercurrent (STCC) is a narrow eastward jet on the equator side of a subtropical gyre, flowing against the broad westward Sverdrup flow. Together with theories, recent enhanced observations and model simulations have revealed the importance of mode waters in the formation and variability of North Pacific STCCs. There are three distinct STCCs in the North Pacific, maintained by low potential vorticity (PV) that mode waters carry from the north. Model simulations show that changes in mode water ventilation result in interannual to interdecadal variations and long-term changes of STCCs. STCCs affect the atmosphere through their surface thermal effects, inducing anomalous cyclonic wind curl and precipitation along them. Thus, mode waters are not merely passive water masses but have dynamical and climatic effects. For temporal variability, atmospheric forcings are also suggested to be important in addition to the variability of mode waters. STCCs exist in other oceans and they are also flanked by mode waters on their poleward sides, suggesting that they are maintained by similar dynamics.

F. Kobashi (✉)
Faculty of Marine Technology, Tokyo University of Marine Science and Technology, Etchujima 2-1-6, Koto-ku, Tokyo 135-8533, Japan
e-mail: kobashi@kaiyodai.ac.jp

F. Kobashi
Research Institute for Global Change, Japan Agency for Marine-Earth Science and Technology, Yokosuka, Japan

A. Kubokawa
Faculty of Environmental Earth Science, Hokkaido University, Sapporo, Japan

Keywords Subtropical Countercurrent · Subtropical Front · Mode water · Ocean circulation · Climate

1 Introduction

A Subtropical Countercurrent (STCC) is a narrow eastward jet on the equator side of a subtropical gyre, where the barotropic flow is westward as predicted by the Sverdrup theory. Figure 1a shows long-term mean sea surface dynamic height referenced to 1000 dbar and surface zonal geostrophic velocity relative to 400 dbar, based on a high-resolution temperature climatology (adapted from Kobashi et al. 2006). The surface flow has an eastward component broadly even in the southern half of the Sverdrup subtropical gyre (Fig. 1b). Such a broad surface eastward flow is predicted by the modern wind-driven ocean circulation theory based on the ventilated thermocline theory (Luyten et al. 1983) and potential vorticity (PV) homogenization theory (Rhines and Young 1982; Young and Rhines 1982). Embedded in but distinct from the broad weak eastward flow are narrow eastward jets. They are the STCCs that the present study focuses on.

There are three distinct STCCs in the North Pacific (Kobashi et al. 2006). They each accompany a temperature and density front at subsurface depths of about 100–200 m (Uda and Hasunuma 1969). Figure 1a, c show subsurface fronts with surface eastward vertical shears in the subtropical gyre. One is in the latitudinal range of 21–25°N from 130°E to 175°E, tilting slightly to the north as it extends to the east. To the south, another front is identified in the latitudinal range of 19–21°N from 130°E to 180°, slightly veering to the north east of 160°E. The other front is found in the central basin, along about 26°N between 175°E and 160°W. These three fronts with large eastward

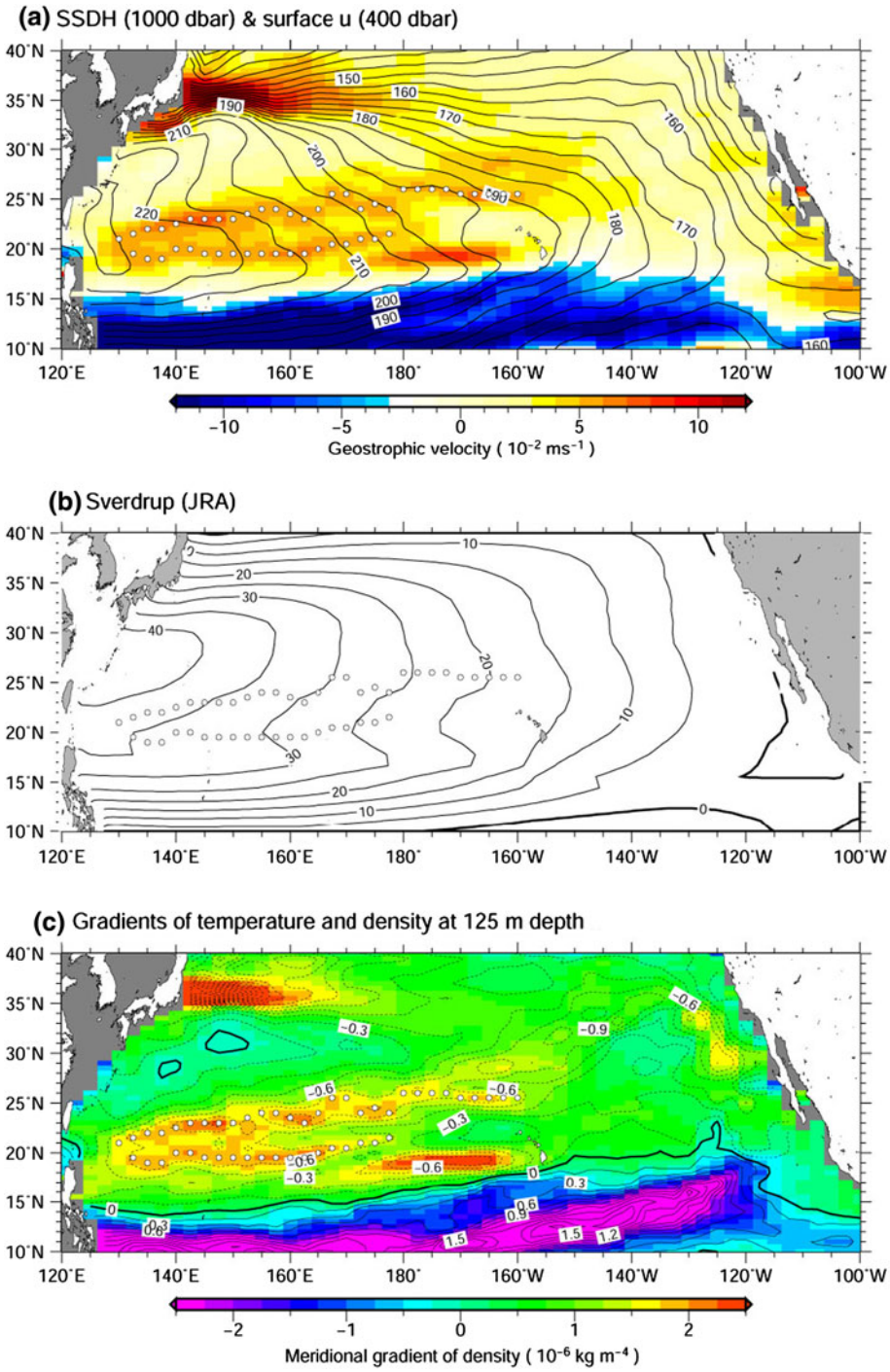

Fig. 1 **a** Long-term mean surface dynamic height referenced to 1000 dbar (contour at 5 cm intervals) and surface zonal geostrophic velocity relative to 400 dbar (*color*). **b** Sverdrup transport streamfunction calculated from long-term mean surface wind stress data of the Japanese 25-year reanalysis (Onogi et al. 2007). **c** Meridional gradients of temperature (contours at 1.0×10^{-5} °C m^{-1} intervals) and density (*color*) at 125 m depth. **a** and **c** are adapted from Kobashi et al. (2006), which are constructed mainly using temperature profiles in the World Ocean Database 2001 (Conkright et al. 2002). *Open circles* in all panels denote the position of STFs defined by Kobashi et al.

current shears exist against the broad southwestward Sverdrup flow (Fig. 1b). In this study, these narrow fronts at subsurface depths and associated currents are called STFs and STCCs, respectively. Following Kobashi et al. (2006), the northern and southern fronts (currents) in the western basin are referred to as the northern and southern STFs (STCCs), respectively, and that in the central basin the eastern STF (STCC).

Another eastward current is found at almost the same latitudes as the southern STCC west of the Hawaiian Islands (Fig. 1a, c), which is called the Hawaiian Lee countercurrent (HLCC). Different from the STCCs, the HLCC is consistent with the Sverdrup flow (Fig. 1b) and driven by Hawaiian Islands-induced wind curls (Xie et al. 2001). In climatology, the HLCC is rather confined in its westward extension up to the dateline (Qiu et al. 1997;

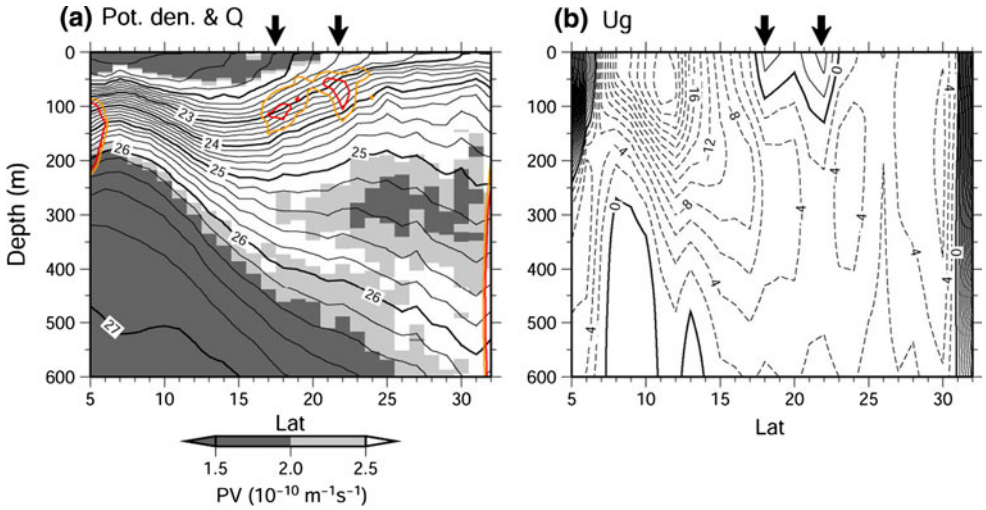

Fig. 2 Mean sections of **a** potential density and **b** zonal geostrophic velocity (referenced to 1000 dbar) along 137°E, calculated from CTD observations in every winter and summer season during 2000–2009, conducted by R/Vs Ryofu Maru and Keifu Maru of the JMA. *Orange* (*red*) contours in **a** denote the meridional gradient of potential density at 2.0 (2.5) $\times$ 10^{-6} kg m^{-4}, and *shade* indicates PV computed from $(f/\rho)(\partial\sigma_\theta/\partial z)$, where f is the Coriolis parameter, ρ is in situ water density, σ_θ is potential density, and z is the vertical coordinate. Stations along the sections are located approximately 1° apart in latitude. The locations of the northern and southern STCCs (STFs) are denoted by *arrows*

Yu et al. 2003; Kobashi et al. 2006), and it is separated from the southern STCC. Although the HLCC is sometimes referred to as "STCC" (e.g., Liu et al. 2003), this study focuses on only STCCs against the Sverdrup circulation.

Figure 2 shows mean meridional sections of potential density and zonal geostrophic velocity (referenced to 1000 dbar) along 137°E. They are calculated from 20 sections of conductivity temperature depth (CTD) observations in every winter and summer during 2000 to 2009, conducted by the R/Vs Ryofu Maru and Keifu Maru of the Japan Meteorological Agency (JMA). The data were obtained from the JMA website. The northern and southern STCCs appear as shallow eastward currents around 22°N and 18°N (Fig. 2b), each with an STF of large meridional temperature gradients at subsurface depths (see color contours in Fig. 2a). The main pycnocline is separated in the subtropical gyre into the upper one sloping up to the north and the lower one sloping down to the north. The STFs are associated with a steep northward shoaling embedded in the gradual shoaling of the upper pycnocline. The slope of the upper pycnocline gives rise to an eastward current shear of the STCCs near the surface by the thermal wind relation.

Since the discovery of STCCs by Uda and Hasunuma (1969), the mechanism of STCC formation has been discussed in a number of studies. Recent studies have revealed the importance of mode waters in the formation of STFs and STCCs, in particular, the subtropical mode water (STMW; Masuzawa 1969) and the central mode water (CMW; Nakamura 1996; Suga et al. 1997). These mode waters originate in the Kuroshio Extension region, where a deep surface mixed layer forms in winter due to intense surface cooling caused by warm water of the Kuroshio Extension being in contact with cold and dry winds of the East Asian monsoon. The deep mixed layer water is subducted into the thermocline and is advected by the wind-driven gyre circulation, producing a thick layer of vertically uniform properties in a wide region of the subtropical gyre. Thus, the mode waters are pycnostads characterized by a vertical minimum in PV. Observational studies have shown that STFs appear along the southern flank of mode waters (Uda and Hasunuma 1969; Suga et al. 1989; Chu et al. 2002; Aoki et al. 2002; Kobashi et al. 2006). For example, in Fig. 2a, the northern and southern STFs are located on the southern flank of the STMW that is identified with a pycnostad around 25.0–25.6 σ_θ between the upper and lower pycnoclines in the subtropical gyre. Similarly, the eastern STF is located along the CMW (Aoki et al. 2002; Kobashi et al. 2006).

In this paper, we review the progress in STCC research. Our understanding has been greatly advanced for the past decades with new developments of satellite and Argo profiling float arrays, accumulation of in situ hydrographic observations, improved numerical modeling, and their use to validate and improve theories. Now we recognize that STCCs are anchored by mode waters, and affect the overlying atmosphere and climate through their surface thermal effects. These findings shed light on the important role of mode waters in ocean current formation and climate. Mode waters are traditionally treated as a topic of water mass analysis, in which the main objective is to understand characteristics of mode waters themselves such

as formation, circulation, and variability, with not much attention being paid to their dynamical and climatic significance. In this paper, we address the following questions that highlight dynamical effects of mode waters: What causes the formation of STCCs? How are STCCs related to mode waters? How do STCCs affect the atmosphere and climate? What causes variability of STCCs? Does variability in mode waters cause that of STCCs?

The remainder of the paper is organized as follows. In Sect. 2, we explain the mechanisms of STCC formation proposed so far. In Sect. 3, following a review of observations of the three STCCs, we estimate their mean surface current velocities. Then, we show how the three STCCs are related to mode waters, followed by a discussion on the mechanisms of their formation. We also describe STCCs simulated by models, and show that they are rather strong compared with those in observations. Section 4 presents atmospheric and climatic effects of STCCs from observations and models. Seasonal to interdecadal variability and long-term change of STCCs and their mechanisms are discussed in Sect. 5, followed by a summary and implications for future studies in Sect. 6.

2 Generation mechanism

In this section, we review four theories: (1) wind-driven mechanism, (2) Ekman convergence mechanism, (3) shock formation of stationary Rossby wave, and (4) vertical accumulation of low PV fluids. Each theory predicts the formation of one STF with STCC. As will be shown in Sect. 3, the observed three STFs are consistent with the mechanisms (3) and (4), both related to mode waters. The mechanisms (1) and (2) turn out not to be essential for the mean STCCs, but seem important for temporal variability (Sect. 4).

2.1 Wind-driven mechanism

Yoshida and Kidokoro (1967a, b) suggested that STCCs are wind-driven currents. They showed that the Sverdrup streamfunction based on the spring wind-stress curl contains an eastward flow between 20°N and 25°N, roughly along the northern and eastern STCCs. This eastward Sverdrup flow is caused by a small-scale trough of anticyclonic wind stress curl in the subtropical gyre. The trough forms only seasonally, and there is no trough in the annual mean wind-stress curl, whereas the northern and eastern STCCs exist in all seasons in observations (Uda and Hasunuma 1969; Kobashi and Kawamura 2002). On the basis of the ocean general circulation model (GCM) driven by wind stress and surface differential heating, Takeuchi (1984) succeeded in reproducing STCC. The wind stress curl used in the experiment has no trough, indicating that the wind-driven mechanism is not essential for STCCs. As will be shown in Sect. 4, Yoshida and Kidokoro's wind curl trough turns out to be due to the STCCs, not the other way round.

2.2 Ekman convergence mechanism

Roden (1975) proposed the hypothesis that STFs are generated by the Ekman convergence between the westerlies and trades. Whether the Ekman convergence produces a front depends on the relative importance of the temperature advection by the Ekman drift to the air–sea heat exchange terms in the temperature equation as discussed by Welander (1981). If we assume that surface heat exchange is proportional to the temperature difference between atmosphere and ocean with constant coefficient k and the oceanic temperature advection is caused by the zonally uniform meridional Ekman transport $V_e = \tau^x/\rho_0 f$, where τ^x is the zonal component of wind stress, ρ_0 is density, and f is the Coriolis parameter, the equation for the mixed layer temperature T in a steady state is

$$V_e(y)\frac{\partial T}{\partial y} = -k[T - T_a(y)], \tag{2.1}$$

where y is the northward coordinate and T_a is the atmospheric temperature which is assumed to depend only on y. The derivation of this equation can be found in Welander (1981). If the Ekman transport $V_e(y)$ and atmospheric temperature $T_a(y)$ are linear functions of y, i.e., $V_e = -\alpha y$ and $T_a = T_0 + \frac{\Delta T}{L} y$, and the domain is $-L/2 < y < L/2$ with the boundary conditions $T = T_0 \pm \Delta T/2$ at $y = \pm L/2$, Eq. 2.1 yields

$$T = T_0 + \frac{k}{k-\alpha}\frac{\Delta T}{L} y - \mathrm{sign}(y)\frac{\alpha \Delta T}{2(k-\alpha)}\left(\frac{2|y|}{L}\right)^{k/\alpha}. \tag{2.2}$$

The meridional gradient of the temperature becomes

$$\frac{dT}{dy} = \frac{k}{k-\alpha}\frac{\Delta T}{L} - \frac{k\Delta T}{L(k-\alpha)}\left(\frac{2|y|}{L}\right)^{k/\alpha - 1}. \tag{2.3}$$

For $0 < k/\alpha \leq 1$, dT/dy is infinite at $y = 0$, and the front becomes weaker as k/α becomes larger. The solution is shown in Fig. 3 for $k/\alpha = 0.5$, 2, 10. Assuming $d\tau^x/dy = 6 \times 10^{-9}$ (dyn cm^{-3}) based on mean wind-stress distribution, we obtain $\alpha \approx 10^{-4}$ (cm s^{-1}) at the 25°N. On the other hand, the coefficient Q_2 of Haney (1971) is 70–100 (ly day^{-1} K^{-1}), which yields $k \approx 10^{-3}$ (cm s^{-1}). From these values, we can estimate $k/\alpha \approx 10$. In this case, there is no front in Fig. 3. Therefore, the Ekman convergence is likely too weak to generate a significant front.

Takeuchi (1984), introduced in Sect. 2.1, also carried out an ocean GCM experiment with meridional wind stress,

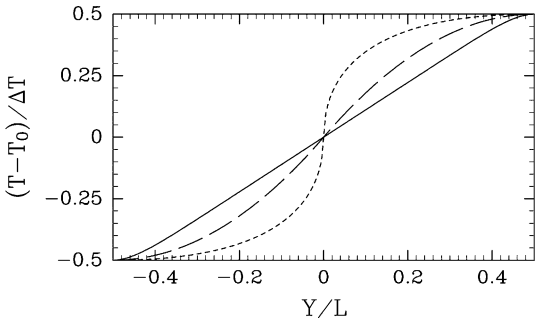

Fig. 3 Meridional distribution of mixed layer temperature given by Eq. 2.2 for $k/\alpha = 0.5$ (*dotted line*), 2.0 (*dashed line*), and 10 (*solid line*)

and obtained STCC very similar to that in the model driven by zonal wind stress. This indicates that the Ekman convergence produced by the westerlies and trades is not essential. In addition, the Ekman convergence occurs between 25°N and 35°N (Roden 1975; Kazmin and Rienecker 1996), slightly to the north of the STCCs, suggesting the same conclusion.

2.3 Shock formation of stationary Rossby wave

The numerical experiments of Takeuchi (1984) strongly suggested that the STCC is wind-driven circulation modified by surface differential heating. Cushman-Roisin (1984) obtained an STF-like structure in a similarity solution to an equation for continuously stratified thermocline (Welander 1959), forced by wind stress and surface differential heating. Although its direct applicability to reality is not clear because it does not satisfy all boundary conditions, the nonlinearity coming from mass conservation produces the STF-like structure. Since the vertical structure is assumed to have a similarity form, the theory may be regarded as that for a single baroclinic mode. Therefore, similar solutions can be obtained in a two-layer system.

Here, we give an explanation of the mechanism of frontogenesis in a two-layer system with some details. The model equation used here is the so-called planetary geostrophic thermocline equation (Dewer 1992) which is based on the hydrostatic balance, geostrophic balance, and mass conservation. The model is driven by the Ekman pumping, in which the total depth H is assumed to be constant, the density difference between two layers is $\Delta\rho$, and mean density is ρ_0. Substituting the geostrophic velocity into the lower layer mass equation, we obtain the equation for the upper layer depth h as

$$\frac{\partial h}{\partial t} - \frac{1}{H} J(\phi, (H-h)/f) - \frac{\beta g'(H-h)h}{f^2 H}\frac{\partial h}{\partial x} = 0, \tag{2.4}$$

where t is time, x and y are the eastward and northward coordinate, respectively, $J(A,B) = A_x B_y - A_y B_x$ is the Jacobian operator, f is the Coriolis parameter, β is df/dy, g' is the reduced gravity ($=\Delta\rho g/\rho_0$), and

$$\phi = \frac{f^2}{\beta}\int_{x_e}^{x} w_e \mathrm{d}x \tag{2.5}$$

is the Sverdrup function. Here, w_e is the Ekman pumping velocity and x_e is the coordinate of the eastern boundary. The coefficient in front of $\partial h/\partial x$ in Eq. 2.4 is the Rossby wave speed. We assume that the model represents the upper ocean whose bottom corresponds to the main thermocline.

The Rossby wave speed in a two-layer system is the highest when $h/H = 1/2$. If $h/H < 1/2$ and $\partial h/\partial x > 0$ or $h/H > 1/2$ and $\partial h/\partial x < 0$ in the initial condition, the Rossby wave front steepens and eventually forms a shock as it propagates westward (Dewar 1987). In a wind-driven circulation, a similar β-induced steepening mechanism can also cause a steady shock (a "spontaneous shock"; Dewer 1992) as explained below.

Assuming a steady state and using the relation

$$J(A,B) = \left[\left(\frac{\partial A}{\partial \phi}\right)_y \left(\frac{\partial B}{\partial y}\right)_\phi - \left(\frac{\partial A}{\partial y}\right)_\phi \left(\frac{\partial B}{\partial \phi}\right)_y\right]\left(\frac{\partial \phi}{\partial x}\right)_y, \tag{2.6}$$

where subscripts denote the variables which are kept constant for differentiation, Eq. 2.4 can be transformed from (x, y) to (ϕ, y) coordinates which is called the Sverdrup coordinate system (Kubokawa 1995):

$$\frac{\partial q}{\partial y} - \beta g'(H - fq)q\frac{\partial q}{\partial \phi} = 0. \tag{2.7}$$

Here $q = (H - h)/f$ is the potential thickness (reciprocal of potential vorticity) of the lower layer. The relation between $x - y$ coordinates and Sverdrup coordinates is shown in Fig. 4. Equation 2.7 is very similar to that for the long Rossby waves; if we set $\phi = 0$ and rewrite Eq. 2.4 using q, the equation for the Rossby wave becomes

$$\frac{\partial q}{\partial t} - \frac{\beta g'(H - fq)q}{fH}\frac{\partial q}{\partial x} = 0. \tag{2.8}$$

Similarity between Eqs. 2.7 and 2.8 allows for an interpretation that the propagation of q on the $\phi - y$ plane is like that on an $x - t$ plane. Since disturbances are advected southward by the Sverdrup flow, $-y$ corresponds to t, and disturbances propagate in the direction of increasing ϕ (westward) on the $\phi - y$ plane as y decreases. Because of the similarity between Eqs. 2.7 and 2.8, we refer to disturbances in 2.7 as stationary Rossby waves. The propagation speed on the $\phi - y$ plane (characteristic speed) is the highest when $fq/H = 1/2$ which is equivalent to $h/H = 1/2$. When $fq/H > 1/2$ ($h/H < 1/2$), the smaller q is,

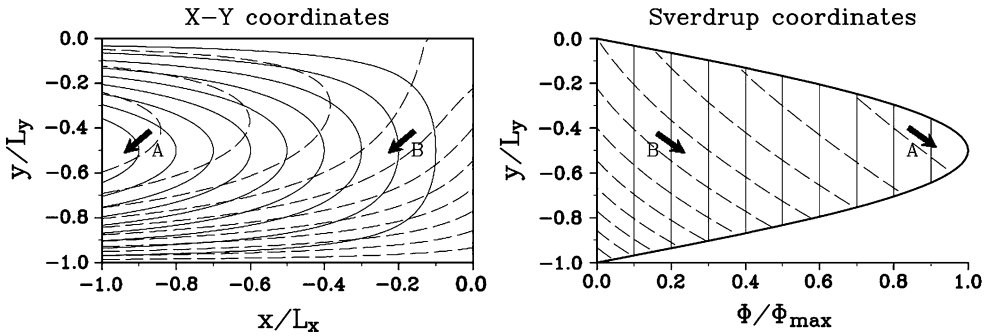

Fig. 4 Relation between the x–y coordinates (*left panel*) and the Sverdrup coordinates (*right panel*). *Solid contours* denote the Sverdrup function, and *dashed contours* the lower layer potential thickness, along which the stationary Rossby wave signals propagate southwestward (*arrows*). The parameters are $\beta L_y/f_0 = 0.5$, $h_e/H = 0.2$ and $\phi_{max}/g'H^2 = 0.2$, where f_0 is the Coriolis parameter at the subpolar–subtropical boundary ($y = 0$) and L_y is the meridional extension of the subtropical gyre, and h_e is the upper layer depth at the eastern boundary. In the present case, the lower layer is at rest. Locations denoted by letters A and B in x–y coordinates correspond to those denoted by the *same letters* in the Sverdrup coordinates. The positive ϕ direction is westward

the higher the speed, and vice versa. Therefore, if q is given along a latitude circle somewhere in the subtropical gyre as satisfying $fq/H > 1/2$ and $\partial q/\partial\phi > 0$ or $fq/H < 1/2$ and $\partial q/\partial\phi < 0$, stationary Rossby waves governed by Eq. 2.7 steepen as y decreases; this behavior is almost the same as that of Rossby waves governed by Eq. 2.8 as time goes.

Curves of constant q in Fig. 4 correspond to trajectories (characteristics) of linear stationary Rossby waves. This example is for a case in which the lower layer is at rest. Since the constant q curve slants southwestward on the $x - y$ plane in the southern half of the subtropical gyre, the eastward vertical shear given by $\partial h/\partial y < 0$ corresponds to $\partial h/\partial x > 0$ ($\partial q/\partial\phi > 0$). Since the sign of $\partial q/\partial\phi$ is unchanged along the characteristics, q in the source region must satisfy the condition that $fq/H > 1/2$ ($h/H < 1/2$) and $\partial q/\partial\phi > 0$ ($\partial q/\partial x < 0$, $\partial h/\partial x > 0$) for the stationary Rossby wave to form a shock with eastward upper-layer current. When the shock forms, it is assumed that a very weak diffusion term which is not explicitly included in the above equations prevents the solution from being multi-valued.

There are four possible sources of stationary Rossby waves and shocks. The first one is the outcrop of the lower layer (Dewer 1992). When the outcrop slants northeastward from the west, q of the subducted water becomes smaller toward east because f is large where the subduction occurs. This structure ($\partial q/\partial x < 0$) steepens as it is advected southward, and a front associated with the eastward current appears in the southern part of the subtropical gyre. The second possible source is the subpolar–subtropical gyre boundary (Dewar 1991, 1992). Although there is a stationary Rossby wave solution on the gyre boundary whose westward propagation velocity locally balances with eastward current weakening toward the eastern boundary, it cannot satisfies the condition, $h/H < 1/2$ and $\partial q/\partial x < 0$, for forming an STCC-like current. Only a shock on the gyre boundary can satisfy this condition. This shock extends into the subtropical gyre, forming an eastward jet in the southern half of the gyre, which is called an "arrested front" (Dewar 1991). This arrested front solution looks like the countercurrent in Cushman-Roisin (1984) which emanates from the gyre boundary, and we can classify these two solutions into the same category, although the model configurations are different from each other and diabatic forcing is imposed in Cushman-Roisin (1984).

The third possible source is the northern part of the western boundary[1] where ϕ changes from 0 to ϕ_{max} (see Fig. 4b). Since $\partial q/\partial\phi > 0$ is equivalent to $\partial q/\partial y < 0$ along the western boundary, when q decreases northward, the stationary Rossby wave emanating from the western boundary can form a shock. The condition $\partial q/\partial y < 0$ implies that the vertical shear is weak or westward there. Furthermore, according to Kubokawa (1995), for the shock to form in the rectangular basin, the vertical shear there must be westward, which seems unrealistic. The last one is the eastern boundary, which has not been discussed as a source of the stationary Rossby wave. In a usual two-layer system, ventilation does not occur at the eastern boundary because the eastern boundary is treated as impermeable and no interlayer flux is allowed. However, in a continuously stratified ocean model with a meridional gradient in the mixed layer, eastern boundary ventilation is inevitable, because density-driven near-surface eastward flows must turn westward below the surface (Sumata and Kubokawa 2001). The eastern boundary ventilation can be incorporated by permitting nonzero baroclinic component of zonal flow at the eastern boundary (Pedlosky 1984). Figure 5 shows a solution with a shock caused by an eastern

[1] The term "western boundary" in this section means the western boundary of the Sverdrup interior region, but not the real western boundary.

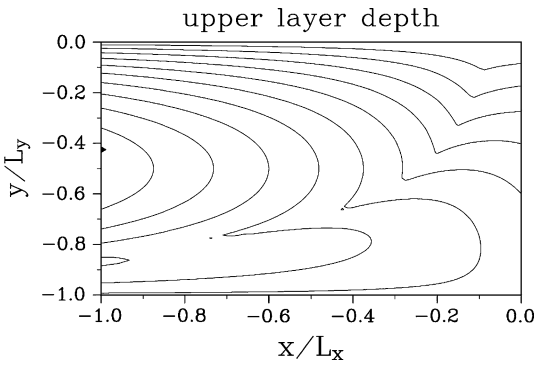

Fig. 5 An example of spontaneous shock solution caused by an eastern boundary ventilation. The *panel* shows the upper layer depth distribution. The parameters are same as those in Fig. 4, but $h_e(y)/H = 0.1 + 0.3\tanh(-2y/L_y)$.

boundary ventilation, in which the thermocline depth at the eastern boundary, $h_e(y)$, is decreasing northward. Since positive $\partial q/\partial y$ along the eastern boundary yields negative $\partial q/\partial x$, the condition for spontaneous shock is satisfied.

In the two-layer model discussed so far, density is constant in each layer. To explore the effects of horizontal density gradient, Kubokawa (1997) presented a theory of a two-level planetary geostrophic model, consisting of equations for vertically integrated density and stratification under the assumptions of geostrophic balance. He discussed the formation of an STCC caused by stationary Rossby waves emanating from the western boundary, and showed that if the density is vertically homogeneous and vertical shear is small at the northwestern subtropical gyre, the stationary Rossby wave can produce a strong countercurrent. Although the mechanism presented by Kubokawa (1997) is essentially the same as that in the two-layer model with western boundary source described above, in the two-level model a stronger countercurrent occurs along the boundary between the regions of weak stratification in the north and strong stratification in the south. Kubokawa (1997) suggested that the northern STF in the real ocean has a similar density structure as in the model, and the homogeneous fluid in the northwestern subtropical gyre may correspond to STMW. The vertical resolution of this model is, however, too coarse; it is therefore desirable to revisit this problem using a multi-layer or a continuously stratified model for a further discussion.

2.4 Vertical accumulation of low PV fluids

Kubokawa and Inui (1999) carried out a numerical experiment similar to that reported by Takeuchi (1984), and pointed out the importance of distribution of low PV fluid subducted from the intersections of outcrops and a mixed-layer-depth front, which is a narrow transition zone separating shallow and deep mixed layers. The mixed-layer-depth front slants slightly northeastward from the western region of the subtropical gyre, whereas outcrops are almost zonal and slant slightly southeastward. As a result, the density of outcrops intersecting the mixed-layer front increases eastward, meaning that the minimum PV fluids on denser isopycnals are formed in the east, whereas those on lighter isopycnals are formed in the west (Fig. 6). Trajectories of these minimum PV fluids on each isopycnal converge on the horizontal plane as they are advected southward, and the low PV fluids are stacked up vertically and form a thick layer of low PV fluid (Fig. 6). This thick low PV layer causes the upper pycnocline to rise, forming a density front and eastward countercurrent on its southern edge (Fig. 2). Since two-layer models cannot reproduce such a situation, Kubokawa (1999) presented a theory using a multi-layer ideal fluid thermocline model. Kubokawa's theory demonstrates that low PV fluids such as mode waters have an important dynamical effect on surface circulation.

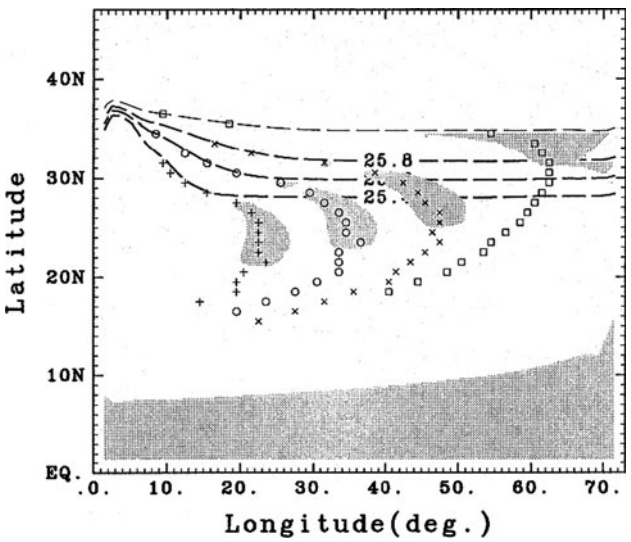

Fig. 6 Trajectories of low PV fluids on four isopycnal surfaces, simulated in an idealized ocean GCM. *Plus symbols*, *open circles*, *multiplication symbols*, and *squares* denote the positions of local minima for given latitudes on the isopycnal surface of 25.4 σ_θ, 25.6 σ_θ, 25.8 σ_θ, and 26.1 σ_θ, respectively. The region with PV lower than 10^{-10} m^{-1} s^{-1} is *shaded*. PV is defined as the same as in Fig. 2. The low PV fluids are vertically stacked up downstream, forming a thick low PV pool, along which STCC appears in the model. From Kubokawa and Inui (1999)

Here, we outline this theory. We write the z-coordinate of the bottom of the j-th layer as $z_j(<0)$, numbering the layers upward from the deepest, with layer 1 being the deepest moving layer and z_0 being constant in space and time, to layer N being the uppermost layer. The sea surface is at $z = 0$ and the density of the j-th layer is ρ_j. Under the planetary geostrophic assumption, conservation of the PV in the n-th layer ($n < N$) can be written as

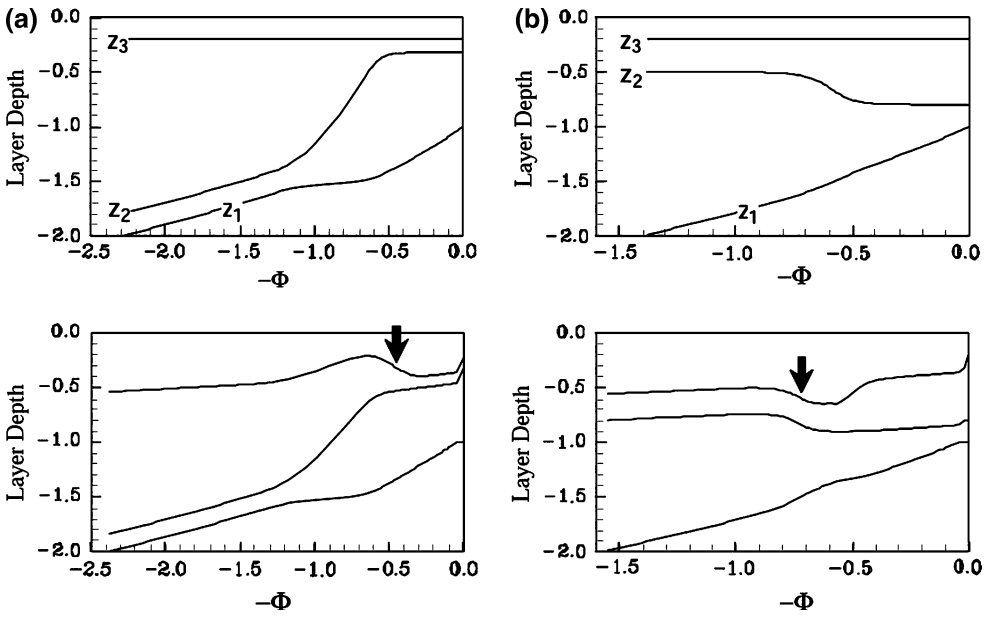

Fig. 7 Two examples of solutions in a 3.5-layer model. Column **a** is for a case in which PV in the deepest moving layer decreases eastward whereas that in the second layer decreases eastward, and column **b** is for a case in which PV in the deepest moving layer decreases westward. The *upper panels* show given zonal distributions of interface depths, z_1, z_2, and z_3 at $f = f_0$, and the *lower panels* show z_1, z_2, and z_3 at $f = 0.8f_0$, calculated by Eqs. 2.12–2.14. The *horizontal axis* $-\phi$ is proportional to $x - x_e$ if w_e is independent of x, i.e., $-\phi = (f^2/\beta)|w_e|(x - x_e)$. z_j values are normalized by z_{01}, and ϕ is normalized by $\gamma_1 z_{01}^2$. γ_j values are assumed to be $\gamma_2/\gamma_1 = \gamma_3/\gamma_1 = 0.5$. *Arrows* are guides for the position of STCC

$$J\left(\sum_{j=1}^{n}\gamma_j z_j, (z_{n+1} - z_n)/f\right) = 0, \tag{2.9}$$

where $\gamma_j = g(\rho_{j-1} - \rho_j)/\rho_0$. For the uppermost layer ($j = N$),

$$-J\left(\sum_{j=1}^{N}\gamma_j z_j, z_N/f\right) = w_e = \frac{\beta}{f^2}\frac{\partial\phi}{\partial x}, \tag{2.10}$$

where ϕ is the Sverdrup function defined by Eq. 2.5. The sum of these equations from $n = 1$ to N yields

$$\frac{\partial}{\partial x}\left(\sum_{j=1}^{N}\frac{\gamma_j}{2}z_j^2\right) = \frac{\partial\phi}{\partial x}, \tag{2.11}$$

which is the Sverdrup relation. Integrating with respect to x from the eastern boundary x_e to x, we obtain

$$\sum_{j=1}^{N}\gamma_j\left(z_j^2 - z_{0j}^2\right) = 2\phi, \tag{2.12}$$

where z_{0j} is the z_j at the eastern boundary.

If the flow in layer 1 is southward, $z_1$is an increasing function of x, and it can be used as a zonal coordinate in place of x. This transformation can be done by the same as that from (x, y) to (ϕ, y) coordinates (see Eq. 2.6), and the equation for the first layer, Eq. 2.9 with $n = 1$, becomes

$$\left(\frac{\partial}{\partial y}\left\{\frac{z_2 - z_1}{f}\right\}\right)_{z_1} = 0, \tag{2.13}$$

where subscript denotes the variable which is kept constant for differentiation. This equation indicates that potential thickness, $(z_2 - z_1)/f$, is constant along lines of constant z_1.

The equation for the second layer becomes

$$\left[\gamma_1 + \gamma_2\left(\frac{\partial z_2}{\partial z_1}\right)_y\right]\left(\frac{\partial}{\partial y}\left\{\frac{z_3 - z_2}{f}\right\}\right)_{z_1} - \gamma_2\left(\frac{\partial z_2}{\partial y}\right)_{z_1}\left(\frac{\partial}{\partial z_1}\left\{\frac{z_3 - z_2}{f}\right\}\right)_y = 0, \tag{2.14}$$

where $\gamma_2\left(\frac{\partial z_2}{\partial y}\right)_{z_1}$ in the second term represents the zonal velocity relative to the first layer. If the velocity in the first layer has a southward component, $z_2 - z_1$ decreases as the fluid column flows southward because of the PV conservation. This implies that interface z_2 tends to deepen southward along the z_1 contour (streamline of the first layer), and this northward inclination of the interface z_2 strengthens the eastward shear. In this way, the current vector tends to rotate counterclockwise with decreasing depth in the subtropical gyre. This tendency is called β-spiral (Stommel and Schott 1977), and implies that the relative location of low PV waters in different layers changes as the water masses flow southward. If low PV fluids in different layers stack vertically, a thick (low PV) layer forms.

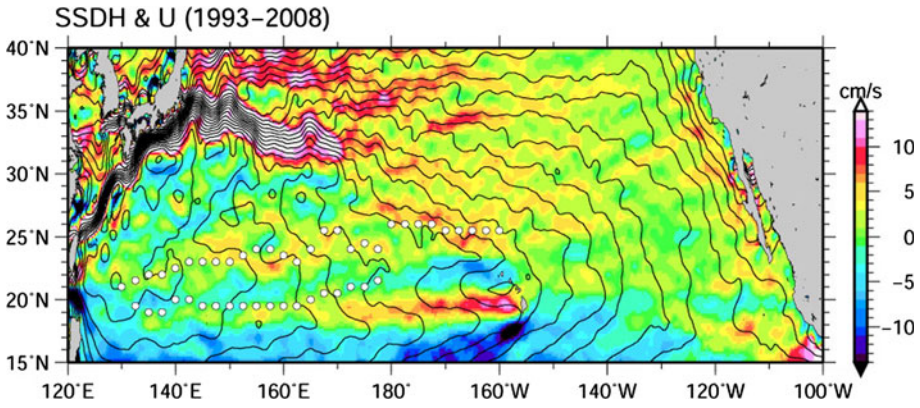

Fig. 8 Absolute mean dynamic height during 1993–2008, computed from an AVISO altimetry product. *Color* indicates eastward geostrophic velocity and *open circles* denote the position of STFs defined by Kobashi et al. (2006)

Figure 7a shows the change of layer thickness distributions in two zonal sections in a 3.5-layer model, in a case that PV in layer 1 decreases eastward whereas that in layer 2 decreases westward in the northern section (upper panel). This PV distribution in the zonal section mimics that in the numerical experiment shown in Fig. 6 (Kubokawa and Inui 1999), in which the PV distribution is caused by the northeastward slanting mixed-layer-depth front. Since the thick low PV fluid in the deep layer moves westward faster than that in the shallower layer, low PV fluid in layer 2 goes on top of that in layer 1 as it is advected southward. In this way, $z_3 - z_1$ increases locally and pushes up the upper interface z_3 (lower panel). This ridge in z_3 extends from northeast to southwest. On the southeastern slope of the ridge in z_3, the eastward current in thermal wind balance occurs (see arrow in Fig. 7a). This is the STCC in Kubokawa (1999). When PV in layer 1 decreases westward whereas PV in layer 2 decreases eastward in the northern zonal section (Fig. 7b), the horizontal positions of high PV regions in layers 1 and 2 get closer as they are advected southward, making a trough in the interface z_3. In this case, an eastward flow occurs along the northwestern slope of the trough (see arrow in Fig. 7b). This case can also occur if the mixed-layer-depth front slants southeastward from the west as shown in Kubokawa (1999).

3 Three STFs

In this section, we first review observations of the three STCCs, and estimate their mean surface current velocities. Then, we show how the three STFs are related to mode waters, followed by a discussion on the mechanisms of their formation. We also show STCCs simulated in models, and discuss their correspondence to the observed STCCs.

3.1 Distribution and mean surface current velocity

Until recently STFs were not fully surveyed. This is partly because of high eddy variability in the STCC regions (e.g., Kawamura et al. 1995; Aoki and Imawaki 1996; Qiu 1999; Kobashi and Kawamura 2001; Hwang et al. 2004). STCCs form a vertically sheared current system with an underlying wind-driven westward flow (Fig. 2b), causing enhanced eddy production through baroclinic instability (Qiu 1999; Kobashi and Kawamura 2002; Noh et al. 2007). The high eddy variability often makes it difficult to describe the details of STCCs from one-time synoptic observations. In addition, because of sparse hydrographic observations, early climatology maps were not able to resolve narrow STCCs, but, instead, they depicted a single broad eastward flow (e.g., Wyrtki 1975; White et al. 1978; Reid and Mantyla 1978), due to strong spatial smoothing of sparse observations.

The three STFs shown by Kobashi et al. (2006) agree in location with previous findings from high resolution observations and climatologies. The northern and southern STFs have been depicted by hydrographic observations (Nitani 1972; Hasunuma and Yoshida 1978; White and Hasunuma 1982; White and Walker 1985; Kaneko et al. 1998; Aoki et al. 2002; Kobashi and Kawamura 2002), and by other observations from surface drifters (Michida 1997), acoustic Doppler current profilers (Ichikawa et al. 2004), and satellite altimetry (Kobashi and Xie 2012). The eastern STF has also been shown from hydrographic observations (Reed 1970; Roden 1980b; White et al. 1978; White and Walker 1985; Aoki et al. 2002; Kobashi and Kawamura 2002).

The three STCCs are identified in absolute mean sea level maps based on satellite altimeter observations (e.g., Niller et al. 2003; Rio and Hernandez 2004; Vianna and Menezes 2010). Figure 8 shows mean ocean dynamic height during 1993–2008, calculated from an altimeter product from Archiving, Validation and Interpretation of Satellite Oceanographic data (AVISO), France. Mean dynamic height used by AVISO is produced by combing satellite altimetry, in situ measurements, and a geoid model (Rio et al. 2011). The northern and eastern STCCs appear clearly along their positions shown by Kobashi et al. (2006), and they are separated around 170–175°E. The

southern STCC, on the other hand, is not obvious but identifiable with small patches of eastward velocity in the general background of westward flow.

We estimated the mean surface velocity of the STCCs based on Fig. 8. By averaging zonal geostrophic velocity zonally between 135°E and 165°E and 180° and 160°W, we obtained the mean velocities as about 3 cm s^{-1} at the northern STCC at 23°N, 1 cm s^{-1} at the southern STCC at 19°N, and 5 cm s^{-1} at the eastern STCC at 26.5°N. These mean velocities agree approximately with those estimated from climatology of sea surface dynamic height based on hydrographic observations (Fig. 2a in Kobashi and Kawamura 2002). In contrast, they are remarkably smaller than those from synoptic hydrographic observations, in which surface velocity of greater than 20 cm s^{-1} is reported at the northern and southern STCCs (Uda and Hasunuma 1969; Kaneko et al. 1998; Aoki et al. 2002). The discrepancy is probably due to eddy contamination in synoptic observations, because mesoscale eddies in the STCC regions have large advective speed of about 20 cm s^{-1} at the surface (Kobashi and Kawamura 2001), several times greater than the mean velocity of the STCCs. This indicates that the mean STCCs tend to be masked by eddies at an instantaneous field.

Judging from the sea surface dynamic height contours in Figs. 1a and 8, we note an interesting feature that the surface geostrophic velocity vector points eastward or southeastward, whereas the band of the STCCs extends to the east or slightly to the northeast, which suggests that the current velocity vector does not follow the direction of the STCCs. STCCs in the theories mentioned in Sect. 2 also show a similar feature. On this point, STCCs are not "currents" in the usual sense of the word, but they are narrow bands of eastward-velocity anomaly.

3.2 Relation to mode waters

The mechanisms in Sects. 2.3 and 2.4 relate STFs to mode waters. Together with Aoki et al. (2002), Kobashi et al. (2006) revealed a close relationship between the STFs and two mode waters, STMW and CMW, from hydrographic observations. Figure 9 shows climatological mean PV on isopycnal surfaces of 25.4 σ_θ, 26.0 σ_θ, and 26.4 σ_θ with acceleration potential relative to 1000 dbar superimposed. These isopycnal surfaces correspond to those of STMW and the upper and lower portions of CMW. A schematic summary is shown in Fig. 10. Both figures are adapted from Kobashi et al.

The three STFs are all located along the southern flank of low PV waters in the thermocline (Fig. 9). Dynamically, meridional slopes of isopycnal surfaces of the STFs are related to large negative meridional PV gradients along isopycnals in the thermocline below the fronts (Fig. 2a;

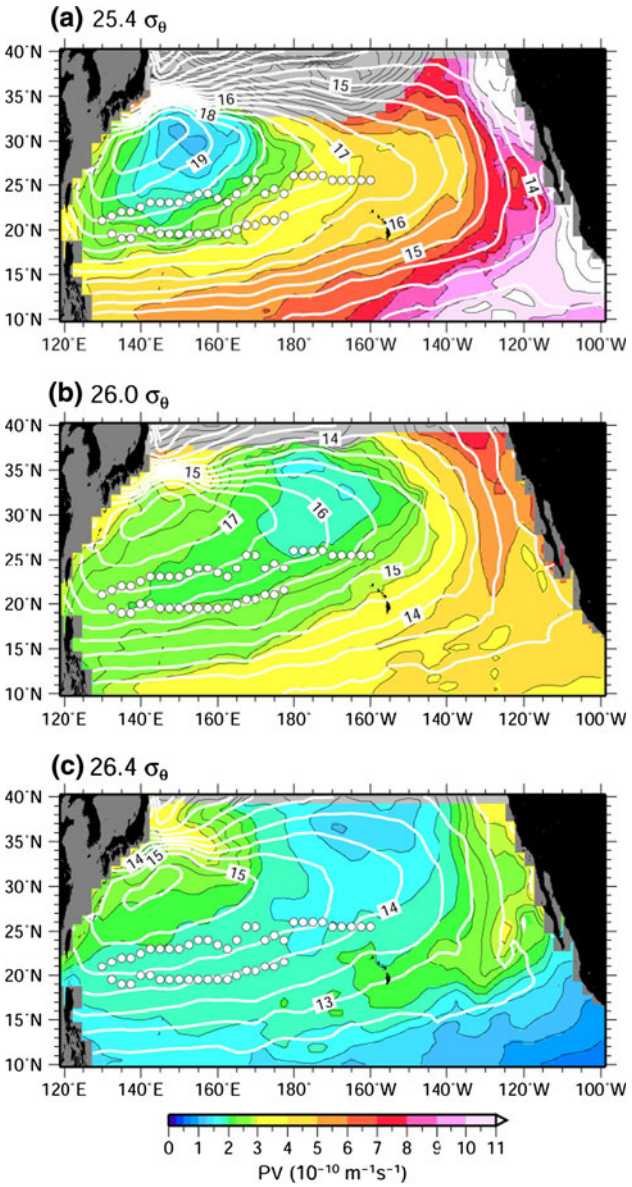

Fig. 9 Map of long-term mean PV on the isopycnal surfaces of **a** 25.4 σ_θ, **b** 26.0 σ_θ, and **c** 26.4 σ_θ. PV is defined as the same as in Fig. 2. Acceleration potential relative to 1000 dbar is shown by *white contours* with an interval of 0.5 m^2 s^{-2}. *Light shade* indicates the area with the winter sea surface density heavier than each isopycnal, and *open circles* denote the STFs. Modified from Kobashi et al. (2006)

Kobashi et al. 2006). The northern STF is located on the southern edge of the Kuroshio recirculation, where the negative meridional PV gradient occurs within a narrow density range and is maintained by the low PV core of STMW (Figs. 9a, 10a). On the other hand, the negative PV gradient at the eastern and southern STFs spans over a wide density range. For the eastern STF, the upper and lower portions of CMW, which are advected along the inner and outer parts of the subtropical gyre, respectively (Oka and Suga 2005), converge to the north of the front, forming a thick low PV layer and maintaining the PV gradient at the

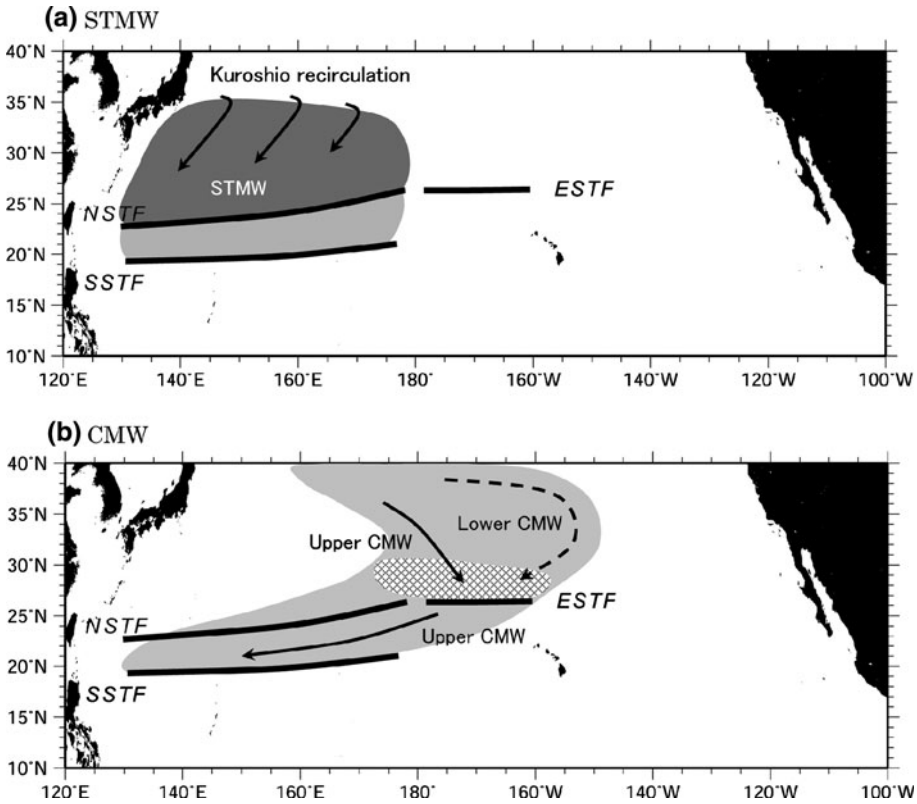

Fig. 10 Schematic of the relationship between STFs and **a** STMW and **b** CMW. The mode waters are represented by *shading*, whereas the northern, southern, and eastern STFs by *thick lines with labels* "NSTF", "SSTF" and "ESTF", respectively. *Arrows* in the *upper panel* indicate the advection of the STMW by the Kuroshio recirculation, whereas *solid and dashed arrows* in the *lower panel* represent the advection of the upper and lower CMWs by the geostrophic gyre flow. The area where the upper and lower CMWs converge is hatched in the *lower panel*. From Kobashi et al. (2006)

front (Figs. 9b, c, 10b). Similarly, at the southern STF, the negative PV gradient is due to a low PV layer to the north, with the southernmost portion of STMW stacked above the upper CMW advected from the central subtropical gyre. The thick low PV waters forces the upper thermocline to shoal, causing surface-intensified STCCs by the thermal wind relation.

The upper CMW extends across the eastern STF to the southwest, almost following streamlines (Fig. 9b), indicating advective spreading by geostrophic flow. On the other hand, the southward spread of low PV across the northern STF in the STMW layer is due to more than just mean flow advection. In Fig. 9a, there are indications that low PV of the STMW south of the northern STF is diffused from a low PV core from the north across the streamlines, possibly by intensive mesoscale eddies in the STCC region. The eddy activity is strongest along the northern STF, and remarkably decreases to the south of the southern STF (Qiu 1999; Kobashi and Kawamura 2002). Eddy transport of STMW across the mean flow is indicated from an analysis of eddy-resolving ocean GCM simulations by Nishikawa et al. (2010). The similar diffusive feature is identified also on maps of PV and streamfunction relative to 2000 dbar produced by Suga et al. (2004) using an isopycnally averaged climatology (their Fig. 5). Thus, the vertical stacking of the mode waters along the southern STF is caused by not just geostrophic advection of the upper CMW but also eddy diffusion of low PV from the STMW core north of the northern STF.

The vertical stacking of low PV waters over a wide density range at the eastern and southern STFs supports the mechanism due to vertical accumulation of low PV fluids in Sect. 2.4 (Kubokawa 1999; Kubokawa and Inui 1999). For the northern STF, the PV gradient is provided mainly by the STMW core to the north advected by the Kuroshio recirculation gyre. As suggested by Aoki et al. (2002), because the STMW resembles a homogeneous water mass in the northwestern subtropical gyre in the theoretical model of Kubokawa (1997), the northern STF could be generated by the stationary Rossby wave mechanism in Sect. 2.3. In addition, the STMW forms progressively eastward on denser isopycnals (Suga and Hanawa 1990), and in the Kuroshio recirculation, lighter STMW stacks above denser STMW (e.g., Bingham 1992; Suga et al. 2004; Oka et al. 2011). The PV gradient at the northern STF occurs in the density range of the STWM (Kobashi et al. 2006). This vertical stacking of the STMW is consistent with Kubokawa's (1999) mechanism. Further examination will be needed to clarify which mechanism is important in the formation of the northern STF.

STCC anchored by mode waters is also simulated by idealized ocean GCMs (Kubokawa and Inui 1999; Endoh et al. 2006) and realistic ocean and coupled GCMs (Yamanaka et al. 2008; Tokinaga et al. 2009a; Xie et al. 2011;

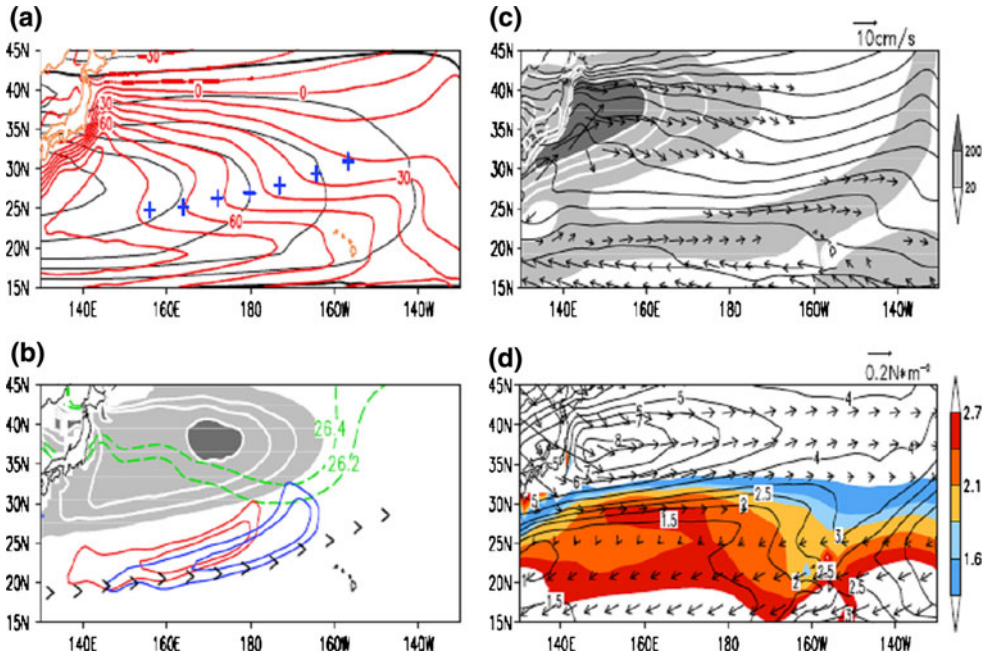

Fig. 11 March climatology from the GFDL coupled model (CM2.1). **a** Annual-mean Sverdrup streamfunction (*black contours* at 20 Sv intervals), SSH (*red contours* at 10 cm intervals), and *plus symbols* denote where a PV minimum is reached in the layer of 25.6–26.6 σ_θ. **b** PV on 26.2 σ_θ (*blue contours*) and 26.4 σ_θ (*blue contours*) isopycnals, along with the mixed layer depth (*light and dark shades* >100 and 400 m; *white contours* at 100 m intervals), surface density (*green*), and ">" symbols denote the axis of STCC. **c** 50 m current velocity, SST (*black contours* at 2°C intervals), and net surface heat flux (*gray shade*; *white contours* at 60 W m^{-2} intervals). **d** Surface wind stress (N m^{-2}), Ekman pumping velocity (*color shade* at 1.0×10^{-6} m s^{-1} intervals), and precipitation (*black contours* at 0.5 kg m^{-2} s^{-1}). From Xie et al. (2011)

Xu et al. 2012; Nonaka et al. 2012). Figure 11 displays the result from a 300-year control simulation from the Geophysical Fluid Dynamics Laboratory (GFDL) coupled climate model (CM2.1), shown by Xie et al. (2011). The model reproduces a narrow eastward jet extending from the western Pacific to the northeast of Hawaii, against the Sverdrup flow (Fig. 11a, c). This STCC agrees in location roughly with the observed southern and eastern STCCs (Fig. 1a), with a notable difference. The observed eastern STCC extends nearly zonally, but in the model the band of the eastern STCC tilts northeastward and apparently is continued from the southern STCC. Low PV waters subducted from the intersections of outcrops and a mixed-layer-depth front are advected by the subtropical gyre, forming the tongues of PV minimums on isopycnal surfaces to the southwest (Fig. 11b). They are vertically stacked up, resulting in a thick low PV layer, along which the STCC forms (Fig. 11b), consistent with observations.

Compared with observations, in the coupled climate models of the CM2.1, analyzed by Xie et al. (2011) and Xu et al. (2012), and the Community Climate System Model (CCSM3.0), analyzed by Tokinaga et al. (2009a), the STCC is too strong (compare Figs. 8 with 11c) as a result of too strong mode waters (Xie et al. 2011). Non-eddy-resolving models tend to produce enhanced mode waters (e.g., Ladd and Thompson 2001; Thompson and Cheng 2008).

In contrast, eddy-resolving ocean GCMs, the Meteorological Research Institute Community Ocean Model (MRI.COM) analyzed by Yamanaka et al. (2008), and the Ocean GCM for the Earth Simulator (OFES) by Nonaka et al. (2012) simulate the eastern STCC with a strength comparable to or slightly weaker than that in observations. In these models, the STCC is more confined to the central subtropical gyre as the eastern STCC, and the southern STCC does not appear in those models, probably due to mixing effect of eddies. Low PV tongues subducted from the central subtropical gyre (Fig. 11b) are much more diffused by eddies as they begin their excursion downstream, resulting in the weaker STF and STCC to the west. The eastern STCC in the MRI.COM and OFES extends zonally with no notable northeastward tilt, consistent with observations. The difference from the climate models could be attributable to reproducibility of subduction and circulation of CMW that is responsible for the formation of the eastern STCC.

4 Atmospheric and climatic effects

This section addresses the question: How do STCCs affect atmosphere and climate? We first look at observations in which an SST front plays an important role. We discuss

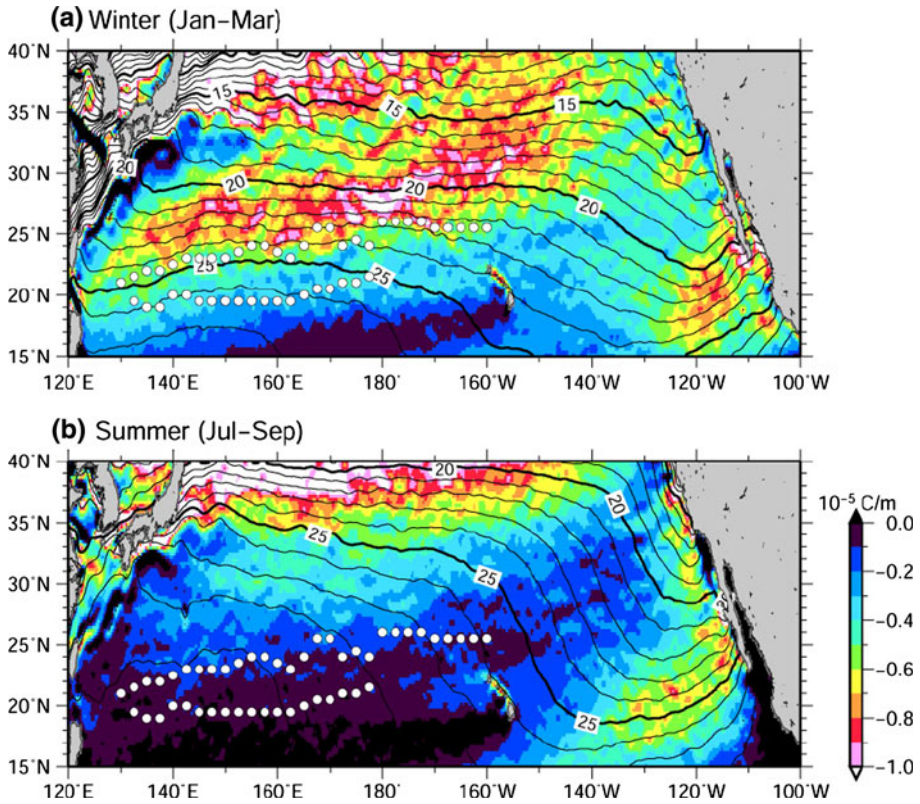

Fig. 12 Seasonal mean SST and its meridional gradient in **a** winter and **b** summer, calculated from an optimally interpolated SST dataset during 1993–2008 (Reynolds et al. 2007). *Open circles* denote the position of STFs defined by Kobashi et al. (2006)

how an SST front is related to subsurface STFs forced by mode waters, and how the SST front affects the atmosphere. Then, we move to results from coupled climate models.

Figure 12 shows seasonal mean SST and its meridional gradient in winter and summer, calculated from an optimally interpolated SST dataset produced from the blend of infrared and microwave satellite observations and in situ measurements (Reynolds et al. 2007). In winter, a pronounced SST front appears in the latitudinal range of 23–35°N, slightly tilting to the northeast, from the western to central subtropical gyre, but it disappears in summer. This SST front is obvious from late fall to early spring (e.g., Roden 1980a). Different from subsurface STFs, the SST front is governed by mixed layer dynamics: its frontogenesis and frontolysis are primarily in response to surface Ekman convergence and surface heat flux (Kazmin and Rienecker 1996; Dinniman and Rienecker 1999). As mentioned in Sect. 2.2, Ekman convergence is too weak to generate a mean STF, but on the seasonal timescale, it could generate an SST front, because k/α changes with season.

To examine the relationship between the SST front and the STFs, we plot the position of the STFs (Kobashi et al. 2006) on Fig. 12. The winter SST front is located along the north of the northern and eastern STFs, and its magnitude rapidly decreases to the south of the STFs. The feature is similar in early spring. This relationship strongly suggests that the SST front is affected not only by Ekman convergence but also by the subsurface STFs. Probably the STFs anchor the SST front above, through an entrainment process in which subsurface temperature anomalies are released to the surface when deep mixed layer develops. Further investigations are needed to reveal the effects of the STFs on the SST front.

A recent finding is that the SST front exerts significant influence on the atmosphere and climate in the western subtropical gyre. From an analysis of QuikSCAT and Tropical Rainfall Measuring Mission (TRMM) satellite observations and reanalysis data from JRA-25, Kobashi et al. (2008) found that, in April to May along the SST front, surface wind stress curls turn weakly cyclonic on the general background of anticyclonic curls that drive the subtropical gyre (Fig. 13). The cyclonic wind curl corresponds to a trough of wind curl shown by Yoshida and Kidokoro (1967a, b), though rather confined to the western subtropical gyre compared with the Yoshida and Kidokoro's trough (see Sect. 2.1). The cyclonic curl anomaly is accompanied by a band of high column water vapor slightly to the south (Fig. 13c), indicating a deep structure of the moist layer. On the weather timescale, the cyclonic curl anomaly is associated with low pressure systems of a subsynoptic scale in space. In the lows, convective rain takes place, with deep upward motion moistening the entire

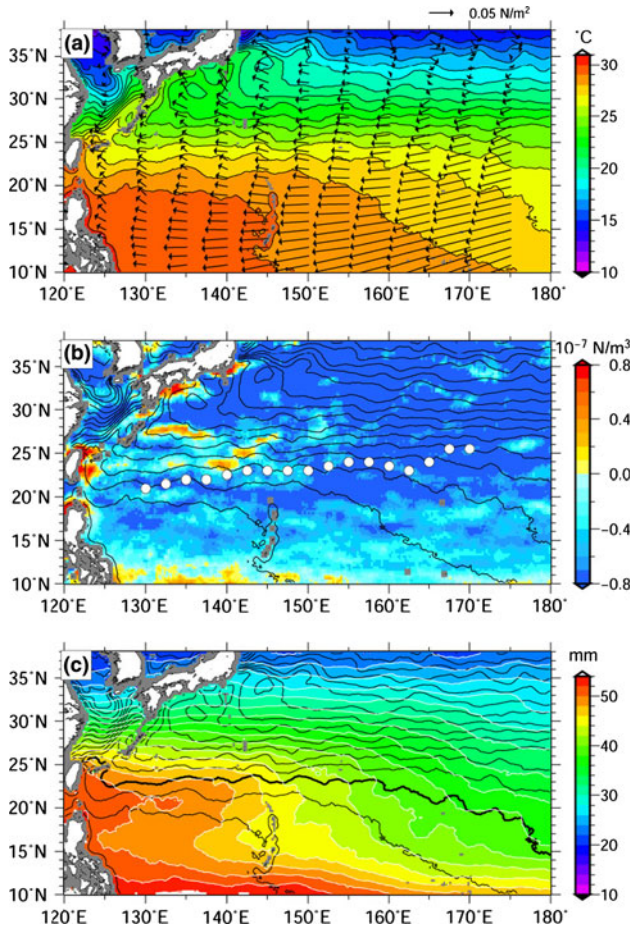

Fig. 13 May climatology from QuikSCAT and TRMM satellite observations: **a** vector wind stress, **b** wind stress curl, and **c** columnar water vapor, along with SST in contours. *Open circles* in **b** denote the position of the northern STF defined by Kobashi et al. (2006). The *thick contour* in **c** marks a 27°C isotherm. Along the SST front near 25°N, a local trough of easterly trade winds (**a**) forms cyclonic wind curl anomaly (**b**). Modified from Kobashi et al. (2008)

troposphere (Fig. 14). The lows are enhanced by condensational heating and grow on the baroclinicity anchored by the SST front, resulting in the formation of cyclonic wind curls on intraseasonal timescales.

Deep atmospheric responses have been recognized in other regions of strong mid-latitude western boundary currents; the Kuroshio Extension (Tokinaga et al. 2009b), the Gulf Stream (Minobe et al. 2008), and the Agulhas Return Current (Liu et al. 2007). Distinct from these western boundary currents, the SST front in the STCC regions is not so strong, but features SST greater than 27°C on its southern flank in April to May (Fig. 13c). This high SST is conducive to deep convection, favoring the formation of cyclonic wind curl anomaly (Kobashi et al. 2008).

The cyclonic wind curl anomaly in May is accompanied by enhanced precipitation. Kobashi et al. (2008) suggested that this increase in precipitation appears to correspond to

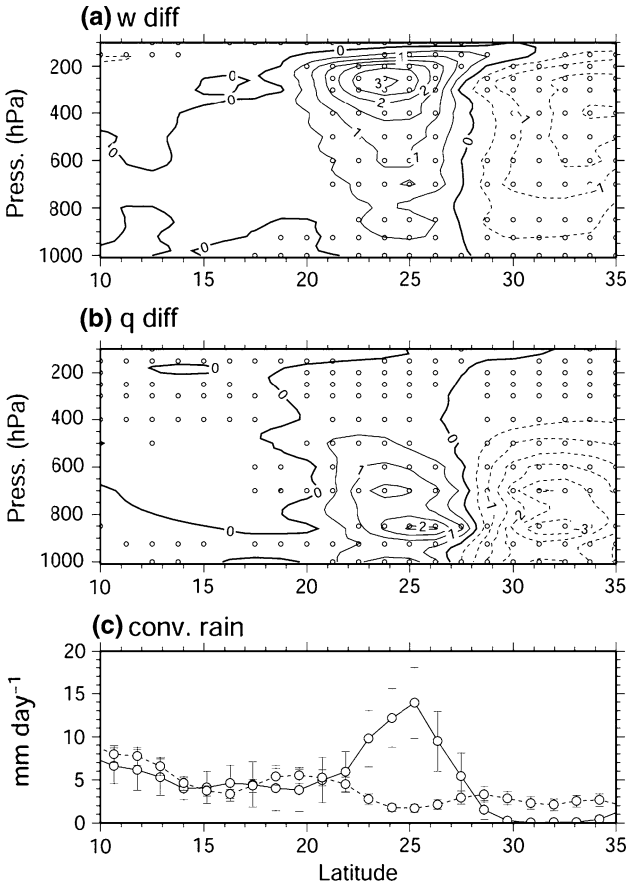

Fig. 14 Composite differences of **a** upward vertical wind (cm/s) and **b** specific humidity (g/kg) at 142.875°E, between the case when cyclonic wind curl appears at the surface and the others. *Open circles* in **a** and **b** show grid points of significant difference with confidence greater than 95%. The vertical wind speed is computed from pressure vertical velocity by the approximate relationship for synoptic scales under hydrostatic approximation. **c** Meridional profiles of convective rain rate (mm/day) in the cyclonic curl (*solid line*) and the other (*dashed line*) composites, along with 95% confidence intervals. These are calculated from JRA-25 data. Along the SST front around 25°N, convective rain takes place with strong upward motion moistening the entire troposphere. Modified from Kobashi et al. (2008)

the so-called pre-Baiu/Meiyu front, which has been independently identified from previous meteorological studies (Kato and Kodama 1992; Tanaka 1992; Wang and LinHo 2002). The pre-Baiu/Meiyu front is manifested as a cloud and rain band prior to the onset of the Baiu/Meiyu that is one of the most remarkable events in the East Asia summer monsoon. The SST front seems to anchor this pre-Baiu/Meiyu band, a hypothesis that needs further investigation.

Atmospheric effects of STCCs are demonstrated in coupled model simulations based on the CCSM3.0 and CM2.1, by Tokinaga et al. (2009a) and Xie et al. (2011), respectively. In these models, the eastern STCC creates an SST ridge via thermal advection (Fig. 11c), forming cyclonic surface wind curls and local maximum of precipitation along the STCC (Fig. 11d). Xie et al. (2011)

suggest that the wind curl response provides a positive feedback on SST via the Sverdrup flow advection mechanism (Liu 1993). The cyclonic wind curl forces a northward Sverdrup flow that acts to strength the SST warming, and the SST warming intensifies the cyclonic wind curl anomalies. This positive feedback is suggested to enhance the coupling between the eastern STCC and the atmosphere.

The atmospheric effect shown by the models differs from that by the observations. In the observations, it results from enhanced atmospheric baroclinicity by the SST front, whereas in the models it is caused by SST anomaly due to thermal advection by the STCC. Recent careful analyses of in situ surface meteorology data and satellite observations find a local peak of net surface heat flux from ocean to atmosphere along the eastern STCC (F. Kobashi and S.-P. Xie, personal communication), suggesting a similar atmospheric response to that of the models. The effect of SST front observed in the western subtropical gyre has not been reported so far from models. Further investigations are needed to clarify the whole picture of atmospheric effects of STCCs and their feedback into the ocean.

The results from the models reveal that mode waters affect atmosphere and climate through surface current formation. This mechanism is different from a previously recognized re-emergence mechanism (e.g., Alexander et al. 1999; Hanawa and Sugimoto 2004; Sugimoto and Hanawa 2005), in which mode waters serve as an isolated heat reservoir memorizing wintertime ocean–atmosphere interaction, modulating local or remote SST by releasing their heat anomalies when deep surface mixed layer develops and entrains mode waters. Mode waters that re-emerge are usually located at subsurface depths in the seasonal thermocline. In contrast, the new mechanism indicates that mode waters that are subducted into the permanent thermocline change surface thermal structure via the surface current formation, affecting atmosphere and climate.

5 Variability and its mechanism

This section addresses the questions: What causes variability of STCCs? Does variability in mode waters cause that of STCCs? Several mechanisms have been suggested, which emphasize the importance of mode waters, atmospheric forcings, and ocean internal dynamics. We review variability of STCCs and its mechanism on seasonal to decadal and longer timescales.

5.1 Seasonal variations

The three STCCs exhibit different seasonal variations. Climatologies of SSH based on hydrographic observations and altimeter observations show that the northern STCC is strong in late winter to spring and weak in fall, whereas the eastern STCC is strong in summer to fall and weak in spring (White et al. 1978; Kobashi and Kawamura 2002; Kobashi and Xie 2012). The southern STCC appears with eastward velocity only in spring to summer (Kobashi and Kawamura 2002), and in winter and fall it is identified as a meridional minimum of westward flow (Kobashi and Xie 2012). Similar seasonal variations of the eastern STCC are also simulated by the OFES (Nonaka et al. 2012).

Mechanisms have not been clarified yet, though there are some implications from observations and numerical simulations. Observations indicate that the strong northern STCC in late winter is caused by a strong SST front (Fig. 12a) with a deep vertical extent within mixed layer depth, whereas that in spring is due to a strengthened subsurface front (Kobashi and Kawamura 2002; Kobashi and Xie 2012). Kobashi and Xie suggest the importance of cyclonic wind stress curl in May along the northern flank of the northern STCC (Fig. 13b). They conducted composite analyses using altimeter-derived surface velocity data, showing that in years with strong cyclonic curl anomaly, the seasonal cycle of the northern STCC is clear with a peak in June, whereas in other years, it is not. In contrast, performing numerical experiments using an idealized ocean GCM, Takeuchi (1986) reproduced seasonal variations similar to those of the northern STCC, suggesting that seasonal change in basin-scale wind stress is important for the seasonal variations of the model STCC.

In climatology, the three STCCs are anchored by mode waters (Sect. 3.2). The STMW, which maintains the northern and southern STCCs, has clear seasonal change in distribution and PV, because of the production of thick STMW in winter and subsequent advection by the Kuroshio recirculation and considerable dissipation within a year or so (Suga and Hanawa 1995). It has not been examined yet whether such seasonal changes of the STMW affect STCC variations. Another possible mechanism is annual Rossby waves (e.g., Mysak 1983; Cummins et al. 1986) that could modulate mode waters and thus induce STCC variations. Seasonal variations could be a superposition of currents forced by atmospheric forcings and mode waters.

5.2 Interannual variations

Interannual variations of the northern STCC are investigated by Qiu and Chen (2010) and Kobashi and Xie (2012). From analysis of satellite observations and JMA repeat hydrographic surveys along 137°E, Qiu and Chen (2010) found interannual changes in mesoscale eddy variability in the northern STCC region, and showed that the vertical shear of the northern STCC tends to be larger in eddy-rich

years than in eddy-weak years. They suggested that the intensity of baroclinic instability controls the interannual changes in the eddy activity. Furthermore, they showed a correlation between the eddy activity and the meridional Ekman convergence associated with basin-scale surface winds, suggesting that the Ekman convergence affects SST frontogenesis along the STCC, causing change in the vertical shear and thus the eddy activity. Their results indicate that Ekman convergence is a cause of interannual variations in the STCC.

On the other hand, Kobashi and Xie (2012) emphasized the importance of a zonal band of cyclonic wind curl in May along the northern flank of the northern STCC (Fig. 13b). From analyses of satellite altimeter data and Argo profiling floats, Kobashi and Xie (2012) found a positive correlation of interannual variations between the cyclonic wind stress curl and the SST front in May, suggesting a positive feedback between them. Furthermore, the cyclonic wind curl is negatively correlated with the SSH and SST below. The strong (weak) cyclonic wind anomaly elevates (depresses) the thermocline and causes the fall (rise) in the SSH and SST, accelerating (decelerating) the northern STCC to the south. The cyclonic wind curl takes a peak in May, followed by the peak of the STCC in June with about 1 month lag. The response of the thermocline to the wind forcing occurs probably locally along the band of the cyclonic wind rather than via Rossby wave propagation. Their results suggest that the wind forcing in May causes the subsequent variations in the northern STCC.

Qiu and Chen (2010) and Kobashi and Xie (2012) both indicate a central role of atmospheric forcings that are not important in the formation of mean STCCs (Sects. 2.1 and 2.2). Their atmospheric forcings are different, but their results are not mutually exclusive. Because eddy production in the northern STCC is seasonally dependent, caused by baroclinic instability in late winter (Qiu 1999; Kobashi and Kawamura 2002), the interannual change in the eddy activity is considered to represent the STCC strength in late winter. Therefore, the result of Qiu and Chen suggests that the Ekman convergence is important for variations in the late winter STCC. Indeed, Kobashi and Xie (2012) suggested that interannual variations of the SST front in late winter are correlated with meridional Ekman convergence forcing. In addition, they found a significant positive correlation between the SST front in late winter and the cyclonic wind curl in May, suggesting that the strong SST front in late winter provides favorable conditions for the development of a strong SST front in spring, affecting the formation of the cyclonic wind curl in May.

Other mechanisms of interannual variations are proposed from an analysis of a long hindcast simulation of the OFES. Nonaka et al. (2012) found that interannual variations of the eastern STCC in the model occur almost simultaneously along a zonal band of the STCC, with a vertically coherent change in current velocity down to at least 1000 m depth. These properties resemble those for zonal jets or striations examined by Richards et al. (2006), suggesting one possibility that they are oceanic internally induced variability, likely caused by geostrophic turbulence. In addition, they found that interannual variations in the near-surface vertical shear of the STCC, which are deviations from the vertically uniform change, are negatively correlated with those in PV of CMW carried to the north of the STCC, indicating that lower PV mode water induces intensified vertical shear of the STCC. They showed that variations in PV of the mode water explain about 20% of interannual variance in zonal velocity of the STCC.

STCC variability due to mode waters has not yet been confirmed from observations. Kobashi and Xie (2012) did a preliminary comparison between changes in STMW thickness and those in strength of the northern STCC using 8-year Argo profiling data in the western subtropical gyre. Apparently, there seems to be no correspondence between them. Although not at STCCs, mode water-induced variations are demonstrated at HLCC by Sasaki et al. (2012). As mentioned in Sect. 1, HLCC is a wind-driven current west of the Hawaiian Islands. Analyzing satellite and Argo float observations, they found that enhanced eastward HLCC in 2003 and 2005 coincided with anomalous southward intrusion of CMW and eastern subtropical mode water (Hautala and Roemmich 1998) to the north of the HLCC. They showed that the intrusion of the mode waters increases the slope of the upper pycnocline, causing the strong HLCC at the surface. An elaborate analysis as done by Nonaka et al. (2012) will be needed to evaluate how interannual variations of STMW and CMW (Suga and Hanawa 1995; Yasuda and Hanawa 1997, 1999; Taneda et al. 2000; Hanawa and Kamada 2001; Hanawa and Yoritaka 2001; Oka 2009) affect STCCs.

5.3 Decadal to longer timescale variations

Mode water-induced variations are dominant on timescales longer than interannual (Nonaka et al. 2012). Model studies showed that changes in ventilation path and core PV of mode water in response to slow variations in wind bring about large subsurface temperature anomalies in the central subtropical gyre (Xie et al. 2000; Kubokawa and Xie 2002; Hosoda et al. 2004). Such changes in mode waters induce variations of STCCs on longer timescales.

Long hindcast simulations by eddy-resolving ocean GCMs indicate that the eastern STCC is intensified in the late 1970s with a strong southward intrusion of CMW to the north of the STCC, and is weakened in the early 1990s

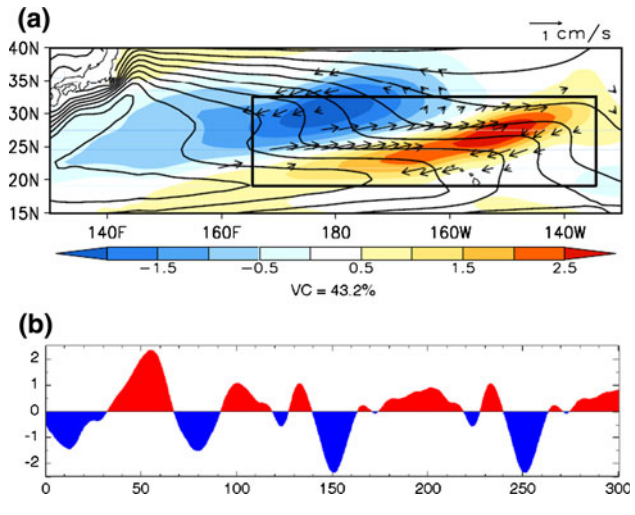

Fig. 15 **a** First empirical orthogonal function (EOF) mode of SSH (*color shade* in cm) in the central-gyre region (*box*), and **b** its principal component, calculated from a 300-year control simulation by the GFDL coupled model (CM2.1). Mean SSH (*black contours* at 10 cm intervals) and regression of 50 m current velocity upon the principal component are superimposed in **a**. From Xie et al. (2011)

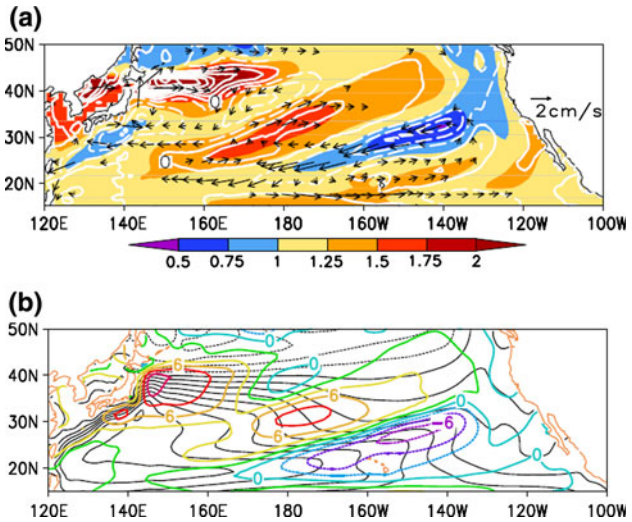

Fig. 16 50-year (2050–2000) changes in March in the A1B global warming simulation by the GFDL climate model (CM2.1): **a** SST (°C), 50 m current velocity (cm s^{-1}), and net surface heat flux (*white contours* at 5 W m^{-2}); SSH change (contours in cm) superimposed on **b** the climatology (*black contours*). From Xie et al. (2011)

when the ventilation of CMW is weak (Yamanaka et al. 2008; Nonaka et al. 2012). Yamanaka et al. related this interdecadal variability to changes in mode water formation and basin-scale wind fields, suggesting that the strong intrusion of the mode water is caused by much more production of CMW due to intensification of the westerly in the mid-1970s (Yasuda and Hanawa 1997), whereas the weak ventilation is associated with the increased warm water advection by the Kuroshio Extension (Hanawa and Kamada 2001) and the eastward shift of mode water formation area, both due to the spin up of the subtropical gyre in a delayed response to the wind intensification.

Changes in mode water ventilation leave characteristic signatures in spatial patterns of surface circulation and SST (Xie et al. 2011; Xu et al. 2012). The interdecadal variability of the eastern STCC is characterized by a northeast-slanted dipole of SSH changes in the central basin (Fig. 15), whose pattern indicates northeastward and southwestward current anomalies by geostrophic balance. The change in the advection of mean SST field produces northeast-slanted bands in SST anomaly fields. Such a pattern with slanted bands is characteristic of SST warming in the North Pacific and North Atlantic subtropical gyres in future projections (Fig. 16; Xie et al. 2010). The global warming reduces the subduction of mode waters in the Kuroshio Oyashio Extension region (Luo et al. 2009; Xu et al. 2012), decelerating the eastern STCC (Xu et al. 2012) and thus causing the slanted bands of changes in surface circulation and SST (Fig. 16). Mode water ventilation is an important mechanism for interdecadal variations as well as changes under global warming.

There is no observational study so far on the decadal variation of STCC. Argo observations have started in 2000, and a large amount of hydrographic data that resolving STCCs and mode waters has been accumulated for the past several years. In the near future, Argo observations will enable us to examine how STCCs are affected by decadal fluctuations in STMW and CMW (e.g., Yasuda and Hanawa 1997; Ladd and Thompson 2002; Suga et al. 2003; Qiu and Chen 2006; Qu and Chen 2009; Sugimoto and Hanawa 2010; Oka and Qiu 2012).

6 Summary and other implications

We have reviewed the progress in studies of the North Pacific STCCs and STFs. Theoretical, observational, and model simulation studies for the past decade have revealed the importance of mode waters in the formation and variability of STCCs. There are three distinct STCCs accompanying subsurface STFs in the North Pacific. They are each anchored by low PV that STMW or CMW carries from the north. The three STCCs support the formation mechanism proposed by Kubokawa (1999) and Kubokawa and Inui (1999), in which the vertical stacking of low PV fluids causes STCCs. Shock formation of stationary Rossby waves (Kubokawa 1997) is also suggested to be important in the formation of the northern STCC. Eddy-resolving ocean models and coupled climate models show that mode waters not only cause the STCCs but also induce variations on interannual to interdecadal timescales and long-term changes in response to global warming. These results

demonstrate that mode water is a dynamical tracer with important consequences for ocean current formation and variability. For temporal variability, atmospheric forcings are also important in addition to the variability of mode waters.

STCC affects the atmosphere and climate. Observations find that the strong SST front in spring along the northern flank of the northern STCC in the western subtropical gyre affects surface wind curl, precipitation, and water vapor content with a deep vertical extent, through generations of low pressure systems of a subsynoptic scale. This observed effect of the SST front has not been confirmed by models. On the other hand, coupled climate models tend to produce another type of ocean–atmosphere interaction, in which the eastern STCC causes the advection of warm water to form an SST anomaly in the central subtropical gyre and affect the atmosphere.

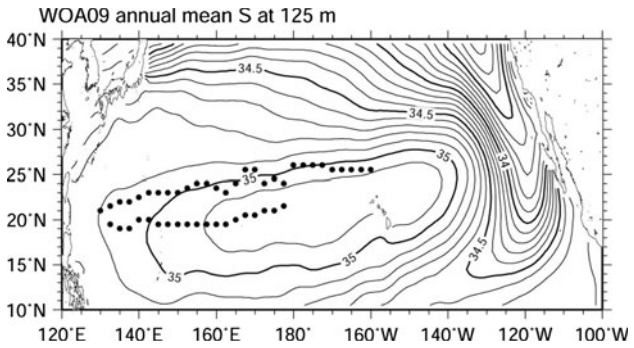

Fig. 17 Annual-mean salinity distribution at depth of 125 m, derived from WOA09. *Black dots* denote the position of STFs defined by Kobashi et al. (2006), the same as those in Fig. 1

These results represent dynamical and climatic effects of mode waters, which are quite different from the traditional view that these water masses act as a heat reservoir with memory of the wintertime ocean–atmosphere interaction. For a fuller understanding of ocean circulation and climate, mode water ventilation and its variability and coupling with the atmosphere are important elements to be considered.

Finally, we discuss some implications for future study. Early observational studies noticed that the northern STF is located not only along STMW to the north but also along the tropical water to the south (Uda and Hasunuma 1969). The North Pacific tropical water is a water mass characterized as a subsurface salinity maximum in the subtropical gyre, which results from the subduction of surface saline water formed by intensive surface evaporation. Previous studies have not paid much attention to salinity effects on STFs, because they have described STFs only from temperature data, using a constant salinity value (White et al. 1978) and salinity estimated from climatological mean temperature and salinity relation (White and Walker 1985; Kobashi and Kawamura 2002; Kobashi et al. 2006).

We plot the position of the STFs (Kobashi et al. 2006) over an annual-mean subsurface salinity map using World Ocean Atlas 2009 data (WOA09; Antonov et al. 2010). Figure 17 is the result, showing that the northern and eastern STFs are located along the northern flank of the tropical water. Indeed, analyses of climatology data (Yuan and Talley 1996) and synoptic observations (Roden 1980b) indicate that STFs are almost collocated with the salinity front. Because temperature and salinity have opposing effects on density, the salinity front weakens the density

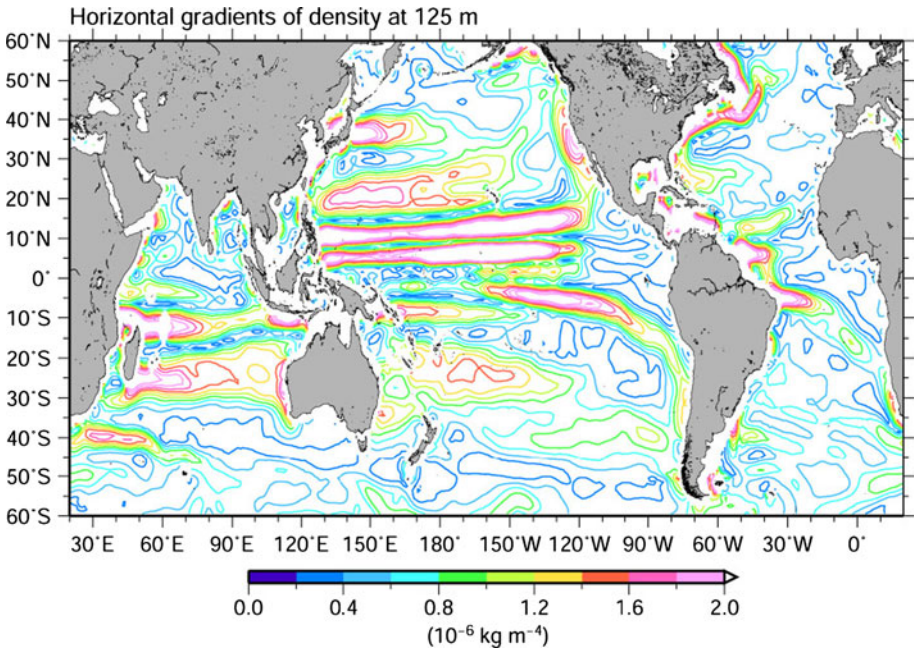

Fig. 18 Magnitude of horizontal gradients of density at depth of 125 m, calculated from annual mean climatology of WOA09

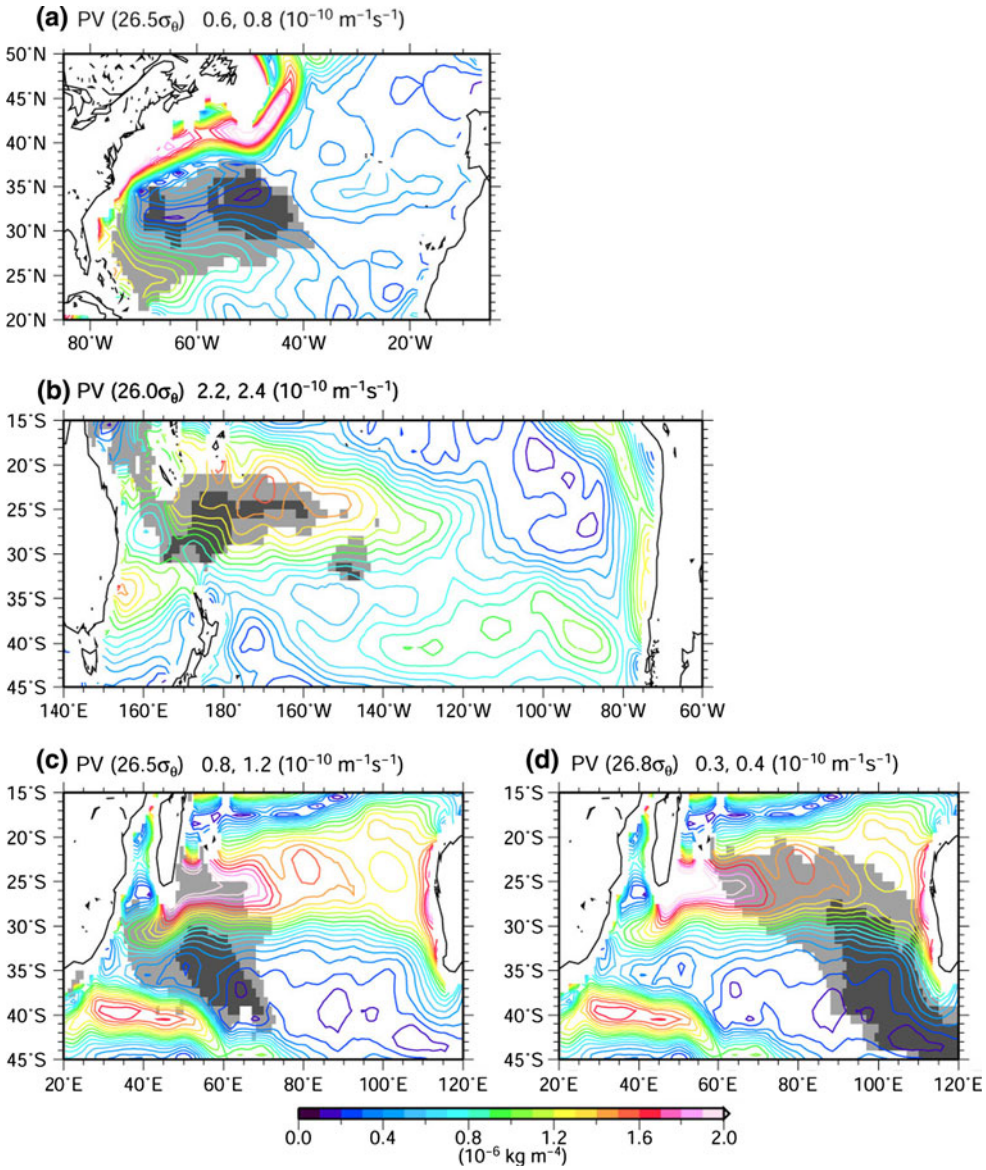

Fig. 19 Isopycnal PV lower than **a** 0.6, 0.8×10^{-10} m^{-1} s^{-1} on 26.5 σ_θ, **b** 2.2, 2.4×10^{-10} m^{-1} s^{-1} on 26.0 σ_θ, **c** 0.8, 1.2×10^{-10} m^{-1} s^{-1} on 26.5 σ_θ, and **d** 0.3, 0.4×10^{-10} m^{-1} s^{-1} on 26.8 σ_θ is highlighted with *light* and *dark shades*, calculated from annual mean climatology of WOA09. PV is defined as the same as in Fig. 2. *Color contours* are the same as in Fig. 18. Low PV water corresponds to **a** North Atlantic STMW, **b** South Pacific STMW, **c** Indian Ocean STMW, and **d** Southeast Indian subantarctic mode water

STFs. It is still unclear how large interannual variability of the tropical water (Suga et al. 2000) affects STCC variations. Accumulation of Argo observations will make it possible to quantitatively estimate salinity effects on STCC variations.

STCC is commonly observed in other oceans, though our knowledge is very limited with regard to the formation, variability, and atmospheric effect. Figure 18 shows the global map of the magnitude of horizontal density gradient at subsurface depth. The magnitude was calculated using $\sqrt{(\partial\rho/\partial x)^2+(\partial\rho/\partial y)^2}$, where ρ is annual mean density computed from WOA09 (Antonov et al. 2010; Locarnini et al. 2010). Strong spatial smoothing of WOA09 data is not ideal for the analysis on narrow bands of STF, but it yields the overall distribution of a broad feature of STF. Indeed, the two bands of STF in the western North Pacific are smoothed out and appear as one broad front in Fig. 18.

In the North Atlantic subtropical gyre, a relatively strong front appears near 25°N east off the Bahamas, extending to the east in the western Sargasso Sea. This front is a subsurface STF associated with eastward current at the surface (e.g., Reid 1978; Olson et al. 1984; Halliwell et al. 1994). In the South Pacific, a prominent zonal band with large density gradients is seen in the latitudes of 20–30°S to the west of 120°W. This front corresponds to an STF, and accompanies a shallow eastward current called the south tropical countercurrent (Merle et al. 1969; Qiu and Chen 2004). A similar broad front is evident in the South Indian Ocean, where the front between 20°S and 30°S extends from the east of Madagascar to the west of Australia. An eastward current associated with this front

was recently identified as the South Indian Ocean countercurrent (Siedler et al. 2006; Palastanga et al. 2007). In the South Atlantic, although STF and its associated countercurrent were reported around 28°S in the western subtropical gyre (Tsuchiya 1985; Me'mery et al. 2000), its signature is not clear in Fig. 16, probably due to the paucity of data and strong smoothing in WOA09.

These STFs seem to be associated with low PV mode water on the poleward side, similar to the North Pacific. With reference to the horizontal distribution of mode waters illustrated by Hanawa and Talley (2001), we examine the possible connection between the STFs and mode waters. Figure 19 displays the isopycnal PV of mode waters, together with the density gradient in Fig. 18. The PV is calculated using WOA09. The STF in the North Atlantic is located along the southern flank of North Atlantic STMW (Worthington 1959), very similar to the northern STF in the North Pacific (Fig. 19a). In the South Pacific, the STF associated with south tropical countercurrent is almost collocated with the South Pacific STMW (Roemmich and Cornuelle 1992; Tsubouchi et al. 2007), and the meridional peak of the front is located slightly to the north of the STMW (Fig. 19b). In the Indian Ocean, the STF seems to be related to two different mode waters (Fig. 19c, d). To the west of the front, the STF is located along the northern flank of the Indian Ocean STMW (Gordon et al. 1987; Tsubouchi et al. 2010), whereas, to the east, it is found along the northern flank of the Southeast Indian subantarctic mode water (Thompson and Edwards 1981). The close relationship in spatial distribution between STFs and mode waters is suggestive of a role of mode waters in eastward current formation. More comprehensive analysis is necessary to reveal the impact of mode waters on global surface circulation and climate.

Acknowledgments We thank Prof. Shang-Ping Xie for many fruitful discussion and comments. Constructive comments from anonymous reviewers greatly helped improve the manuscript. This study is partially supported by Grants-in-Aid for Scientific Research of the Ministry of Education, Culture, Sports, Science and Technology, Japan [20740267, 22106007, 23340139]. The altimeter product was produced by Ssalto/Duacs and distributed by AVISO, with support from CNES. The SST dataset was obtained from the NOAA website.

References

Alexander MA, Deser C, Timlin MS (1999) The reemergence of SST anomalies in the North Pacific Ocean. J Clim 12:2419–2433

Antonov JI, Seidov D, Boyer TP, Locarnini RA, Mishonov AV, Garcia HE, Baranova OK, Zweng MM, Johnson DR (2010) World Ocean Atlas 2009. Salinity, vol 2. In: Levitus S (ed) NOAA Atlas NESDIS 69. US Government Printing Office, Washington, DC

Aoki S, Imawaki S (1996) Eddy activities of the surface layer in the western North Pacific detected by satellite altimeter and radiometer. J Oceanogr 52:457–474

Aoki Y, Suga T, Hanawa K (2002) Subsurface subtropical fronts of the North Pacific as inherent boundaries in the ventilated thermocline. J Phys Oceanogr 32:2299–2311

Bingham FM (1992) Formation and spreading of subtropical mode water in the North Pacific. J Geophys Res 97:11177–11189

Chu PC, Li R, You X (2002) Northwest Pacific subtropical countercurrent on isopycnal surface in summer. Geophys Res Lett 29:1842. doi:10.1029/2002GL014831

Conkright ME, Antonov JI, Baranova O, Boyer TP, Garacia HE, Gelfeld R, Johnson D, Locarnin RA, Murphy PP, O'Brien TD, Smolyar I, Stephens C (2002) World Ocean Database 2001. Introduction, vol 1. In: Levitus S (ed) NOAA Atlas, NESDIS 42. US Government Printing Office, Washington, DC

Cummins PF, Mysak LA, Hamilton K (1986) Generation of annual Rossby waves in the North Pacific by the wind stress curl. J Phys Oceanogr 16:1179–1189

Cushman-Roisin B (1984) On the maintenance of the subtropical front and its associated countercurrent. J Phys Oceanogr 14:1179–1190

Dewar WK (1987) Planetary shock waves. J Phys Oceanogr 17:470–482

Dewar WK (1991) Arrested fronts. J Mar Res 49:21–52

Dewer WK (1992) Spontaneous shocks. J Phys Oceanogr 22:505–522

Dinniman MS, Rienecker MM (1999) Frontogenesis in the North Pacific oceanic frontal zones: a numerical simulation. J Phys Oceanogr 29:537–559

Endoh T, Jia Y, Richards KJ (2006) Sensitivity of the ventilation process in the North Pacific to eddy-induced tracer transport. J Phys Oceanogr 36:1895–1911

Gordon AL, Lutjeharms JRE, Grundlingh ML (1987) Stratification and circulation at the Agulhas retroflection. Deep Sea Res 34:565–599

Halliwell GR Jr, Peng G, Olson DB (1994) Stability of the Sargasso Sea subtropical frontal zone. J Phys Oceanogr 24:1166–1183

Hanawa K, Kamada J (2001) Variability of core layer temperature (CLT) of North Pacific subtropical mode water. Geophys Res Lett 28:2229–2232

Hanawa K, Sugimoto S (2004) 'Reemergence' areas of winter sea surface temperature anomalies in the world's oceans. Geophys Res Lett 31:L10303. doi:10.1029/2004GL019904

Hanawa K, Talley LD (2001) Mode waters. In: Siedler G, Church J (eds) Ocean circulation and climate. International geophysics series. Academic, San Diego, pp 373–386

Hanawa K, Yoritaka H (2001) North Pacific subtropical mode water observed in long cross section along 32.5°N line. J Oceanogr 57:679–692

Haney RL (1971) Surface thermal boundary condition for ocean circulation models. J Phys Oceanogr 1:241–248

Hasunuma K, Yoshida K (1978) Splitting the subtropical gyre in the western North Pacific. J Oceanogr Soc Japan 34:160–172

Hautala SL, Roemmich DH (1998) Subtropical mode water in the Northeast Pacific basin. J Geophys Res 106:19671–19681

Hosoda S, Xie S-P, Takeuchi K, Nonaka M (2004) Interdecadal temperature variations in the North Pacific central mode water simulated by an OGCM. J Oceanogr 60:865–877

Hwang C, Wu C-R, Kao R (2004) TOPEX/Poseidon observations of mesoscale eddies over the subtropical countercurrent: kinematic characteristics of an anticyclonic eddy and a cyclonic eddy. J Geophys Res 109:C08013. doi:10.1029/2003JC002026

Ichikawa K, Gohda N, Arai M, Kaneko A (2004) Monitoring surface velocity from repeated ADCP observations and satellite altimetry. J Oceanogr 60:365–374

Kaneko I, Takatsuki Y, Kamiya H, Kawae S (1998) Water property and current distributions along the WHP-P9 section (137°–142°E) in the western North Pacific. J Geophys Res 103:12959–12984

Kato K, Kodama Y (1992) Formation of the quasi-stationary Baiu front to the south of the Japan Islands in early May of 1979. J Meteor Soc Jpn 70:631–647

Kawamura H, Sawa Y, Sakaida F (1995) Satellite observations of 3–6 months variation in the Kuroshio and the subtropical front. Umi Sora 71:9–15 (in Japanese with English abstract and legends)

Kazmin AS, Rienecker MM (1996) Variability and frontogenesis in the large-scale oceanic frontal zones. J Geophys Res 101:907–921

Kobashi F, Kawamura H (2001) Variation of sea surface height at periods of 65–220 days in the subtropical gyre of the North Pacific. J Geophys Res 106:26817–26831

Kobashi F, Kawamura H (2002) Seasonal variation and instability nature of the North Pacific subtropical countercurrent and the Hawaiian Lee countercurrent. J Geophys Res 107:3185. doi:10.1029/2001JC001225

Kobashi F, Xie SP (2012) Interannual variability of the North Pacific subtropical countercurrent: role of local ocean–atmosphere interaction. J Oceanogr. doi:10.1007/s10872-011-0048-x

Kobashi F, Mitsudera H, Xie S-P (2006) Three subtropical fronts in the North Pacific: observational evidence for mode water-induced subsurface frontogenesis. J Geophys Res 111:C09033. doi:10.1029/2006JC003479

Kobashi F, Xie S-P, Iwasaka N, Sakamoto TT (2008) Deep atmospheric response to the North Pacific oceanic subtropical front in spring. J Clim 21:5960–5975

Kubokawa A (1995) Stationary Rossby waves and shocks on the Sverdrup coordinate. J Oceanogr 51:207–224

Kubokawa A (1997) A two-level model of subtropical gyre and subtropical countercurrent. J Oceanogr 53:231–244

Kubokawa A (1999) Ventilated thermocline strongly affected by a deep mixed layer: a theory for subtropical countercurrent. J Phys Oceanogr 29:1314–1333

Kubokawa A, Inui T (1999) Subtropical countercurrent in an idealized ocean GCM. J Phys Oceanogr 29:1303–1313

Kubokawa A, Xie S-P (2002) On steady response of a ventilated thermocline to enhanced Ekman pumping. J Oceanogr 58:565–575

Ladd C, Thompson L (2001) Water mass formation in an isopycnal model of the North Pacific. J Phys Oceanogr 31:1517–1537

Ladd C, Thompson L (2002) Decadal variability of North Pacific central mode water. J Phys Oceanogr 32:2870–2881

Liu Z (1993) Interannual positive feedbacks in a simple extratropical air–sea coupling system. J Atmos Sci 50:3022–3028

Liu Q, Wang S, Wang Q, Wang W (2003) On the formation of subtropical countercurrent to the west of the Hawaiian Islands. J Geophys Res 108:3167. doi:10.1029/2002JC001366

Liu WT, Xie X, Niiler PP (2007) Ocean–atmosphere interaction over Agulhas Extension meanders. J Clim 20:5784–5797

Locarnini RA, Mishonov AV, Antonov JI, Boyer TP, Garcia HE, Baranova OK, Zweng MM, Johnson DR (2010) World Ocean Atlas 2009. Temperature, vol 1. Levitus S (ed) NOAA Atlas NESDIS 68. US Government Printing Office, Washington, DC

Luo Y, Liu Q, Rothstein LM (2009) Simulated response of North Pacific mode waters to global warming. Geophys Res Lett 36:L23609. doi:10.1029/2009GL040906

Luyten JR, Pedlosky J, Stommel H (1983) The ventilated thermocline. J Phys Oceanogr 13:292–309

Masuzawa J (1969) Subtropical mode water. Deep Sea Res 16:436–472

Me'mery L, Arhan M, Alvarez-Salgado XA, Messias M-J, Mercier H, Castro CG, Rios AF (2000) The water masses along the western boundary of the south and equatorial Atlantic. Prog Oceanogr 47:69–98

Merle J, Rotschi H, Voituriez B (1969) Zonal circulation in the tropical western South Pacific at 170°E. Bull Jpn Soc Fish Oceanogr. Special Number (Prof. Uda's Commemorative Papers), 91–98

Michida Y (1997) Surface current field in the area of subtropical countercurrent observed with surface drifters. Rep Hydro Res 33:21–30 (in Japanese with English abstract)

Minobe S, Kuwano-Yoshida A, Komori N, Xie S-P, Small RJ (2008) Influence of the Gulf Stream on the troposphere. Nature 452:206–209

Mysak LA (1983) Generation of annual Rossby waves in the North Pacific. J Phys Oceanogr 13:1908–1923

Nakamura H (1996) A pycnostad on the bottom of the ventilated portion in the central subtropical North Pacific: its distribution and formation. J Oceanogr 52:171–188

Niller PP, Maximenko NA, McWilliams JC (2003) Dynamically balanced absolute sea level of the global ocean derived from near-surface velocity observations. Geophys Res Lett 30(22):2164. doi:10.1029/2003GL018628

Nishikawa S, Tsujino H, Sakamoto K, Nakano H (2010) Effects of mesoscale eddies on subduction and distribution of subtropical mode water in an eddy-resolving OGCM of the western North Pacific. J Phys Oceanogr 40:1748–1765

Nitani H (1972) Beginning of the Kuroshio. Stommel H, Yoshida K (eds) Kuroshio—its physical aspects. University of Tokyo Press, Tokyo, pp 129–163

Noh Y, Yim BY, You SH, Yoon JH, Qiu B (2007) Seasonal variation of eddy kinetic energy of the North Pacific subtropical countercurrent simulated by an eddy-resolving OGCM. Geophys Res Lett 34:L07601. doi:10.1029/2006GL029130

Nonaka M, Xie SP, Sasaki H (2012) Interannual variations in low potential vorticity water and the subtropical countercurrent in an eddy-resolving OGCM. J Oceanogr. doi:10.1007/s10872-011-0042-3

Oka E (2009) Seasonal and interannual variation of North Pacific subtropical mode water in 2003–2006. J Oceanogr 65:151–164

Oka E, Qiu B (2012) Progress of North Pacific mode water research in the past decade. J Oceanogr. doi:10.1007/s10872-011-0032-5

Oka E, Suga T (2005) Differential formation and circulation of North Pacific central mode water. J Phys Oceanogr 35:1997–2011

Oka E, Suga T, Sukigara C, Toyama K, Shimada K, Yoshida J (2011) "Eddy-resolving" observation of the North Pacific subtropical mode water. J Phys Oceanogr 41:666–681

Olson DB, Schott FA, Zantopp RJ, Leaman KD (1984) The mean circulation east of the Bahamas as determined by a recent measurement program and historical XBT data. J Phys Oceanogr 14:1470–1487

Onogi K, Tsutsui J, Koide H, Sakamoto M, Kobayashi S, Hatsushika H, Matsumoto T, Yamazaki N, Kamahori H, Takahashi K, Kadokura S, Wada K, Kato K, Oyama R, Ose T, Mannoji N, Taira R (2007) The JRA-25 reanalysis. J Meteor Soc Jpn 85:369–432

Palastanga V, van Leeuwen PJ, Schouten MW, de Ruijter WPM (2007) Flow structure and variability in the subtropical Indian Ocean: instability of the South Indian Ocean countercurrent. J Geophys Res 112:C01001. doi:10.1029/2005JC003395

Pedlosky J (1984) Cross-gyre ventilation of the subtropical gyre: an internal mode in the ventilated thermocline. J Phys Oceanogr 14:1172–1178

Qiu B (1999) Seasonal eddy field modulation of the North Pacific subtropical countercurrent: TOPEX/Poseidon observations and theory. J Phys Oceanogr 29:2471–2486

Qiu B, Chen S (2004) Seasonal modulations in the eddy field of the South Pacific Ocean. J Phys Oceanogr 34:1515–1527

Qiu B, Chen S (2006) Decadal variability in the formation of the North Pacific subtropical mode water: oceanic versus atmospheric control. J Phys Oceanogr 36:1365–1380
Qiu B, Chen S (2010) Interannual variability of the North Pacific subtropical countercurrent and its associated mesoscale eddy field. J Phys Oceanogr 40:213–225
Qiu B, Koh DA, Lumpkin C, Flament P (1997) Existence and formation mechanism of the North Hawaiian Ridge current. J Phys Oceanogr 27:431–444
Qu T, Chen J (2009) A North Pacific decadal variability in subduction rate. Geophys Res Lett 36:L22602. doi:10.1029/2009GL040914
Reed RK (1970) On subtropical currents and thermal structure in the central North Pacific. J Oceanogr Soc Japan 26:183–184
Reid JL (1978) On the mid-depth circulation and salinity field in the North Atlantic Ocean. J Geophys Res 83:5063–5067
Reid JL, Mantyla AW (1978) On the mid-depth circulation of the North Pacific Ocean. J Phys Oceanogr 8:946–951
Reynolds RW, Smith TM, Liu C, Chelton DB, Casey KS, Schlax MG (2007) Daily high-resolution blended analyses for sea surface temperature. J Clim 20:5473–5496
Rhines PB, Young WR (1982) A theory of the wind-driven circulation. Part I: mid-ocean gyres. J Mar Res 40(Suppl):559–596
Richards KJ, Maximenko NA, Bryan FO, Sasaki H (2006) Zonal jets in the Pacific Ocean. Geophys Res Lett 33:L03605. doi:10.1029/2005GL024645
Rio M-H, Hernandez F (2004) A mean dynamic topography computed over the world ocean from altimetry, in situ measurements, and a geoid model. J Geophys Res 109:C12032. doi:10.1029/2003JC002226
Rio M-H, Guinehut S, Larnicol G (2011) New CNES-CLS09 global mean dynamic topography computed from the combination of GRACE data, altimetry, and in situ measurements. J Geophys Res 116:C07018. doi:10.1029/2010JC006505
Roden GI (1975) On the north Pacific temperature, salinity, sound velocity fronts, and the relation to the wind and energy flux fields. J Phys Oceanogr 5:557–571
Roden GI (1980a) On the variability of surface temperature fronts in the western Pacific, as detected by satellite. J Geophys Res 85:2704–2710
Roden GI (1980b) On the subtropical frontal zone north of Hawaii during winter. J Phys Oceanogr 10:342–362
Roemmich D, Cornuelle B (1992) The subtropical mode waters of the South Pacific Ocean. J Phys Oceanogr 22:1178–1187
Sasaki H, Xie SP, Taguchi B, Nonaka M, Hosoda S, Masumoto Y (2012) Interannual variations of the Hawaiian Lee countercurrent induced by low potential vorticity water ventilation in the subsurface. J Oceanogr. doi:10.1007/s10872-011-0074-8
Siedler G, Rouault M, Lutjeharms JRE (2006) Structure and origin of the subtropical South Indian Ocean countercurrent. Geophys Res Lett 33:L24609. doi:10.1029/2006GL027399
Stommel H, Schott F (1977) The beta spiral and the determination of the absolute velocity field from hydrographic station data. Deep Sea Res 24:325–329
Suga T, Hanawa K (1990) The mixed layer climatology in the northwestern part of the North Pacific subtropical gyre and the formation area of subtropical mode water. J Mar Res 48:543–566
Suga T, Hanawa K (1995) The subtropical mode water circulation in the North Pacific. J Phys Oceanogr 25:958–970
Suga T, Hanawa K, Toba Y (1989) Subtropical mode water in the 137°E section. J Phys Oceanogr 19:1605–1618
Suga T, Takei Y, Hanawa K (1997) Thermostad distribution in the North Pacific subtropical gyre: the central mode water and the subtropical mode water. J Phys Oceanogr 27:140–152
Suga T, Kato A, Hanawa K (2000) North Pacific tropical water: its climatology, temporal changes associated with the climate regime shift in the 1970s. Prog Oceanogr 47:223–256
Suga T, Motoki K, Hanawa K (2003) Subsurface water masses in the central North Pacific transition region: the repeat section along the 180° meridian. J Oceanogr 59:435–444
Suga T, Motoki K, Aoki Y, Macdonald AM (2004) The North Pacific climatology of winter mixed layer and mode waters. J Phys Oceanogr 34:3–22
Sugimoto S, Hanawa K (2005) Remote reemergence areas of winter sea surface temperature anomalies in the North Pacific. Geophys Res Lett 32:L01606. doi:10.1029/2004GL021410
Sugimoto S, Hanawa K (2010) Impact of Aleutian Low activity on the STMW formation in the Kuroshio recirculation gyre region. Geophys Res Lett 37:L03606. doi:10.1029/2009GL041795
Sumata H, Kubokawa A (2001) Numerical study of eastern boundary ventilation and its effects on the thermocline structure. J Phys Oceanogr 31:3002–3019
Takeuchi K (1984) Numerical study of the subtropical front and the subtropical countercurrent. J Oceanogr Soc Jpn 40:371–381
Takeuchi K (1986) Numerical study of the seasonal variations of the subtropical front and the subtropical countercurrent. J Phys Oceanogr 16:919–926
Tanaka M (1992) Intraseasonal oscillation and the onset and retreat dates of the summer monsoon over East, Southeast Asia and the western Pacific region using GMS high cloud amount data. J Meteor Soc Jpn 70:613–629
Taneda T, Suga T, Hanawa K (2000) Subtropical mode water variation in the northwestern part of the North Pacific subtropical gyre. J Geophys Res 105:19591–19598
Thompson L, Cheng W (2008) Water masses in the Pacific in CCSM3. J Clim 21:4514–4528
Thompson RORY, Edwards RJ (1981) Mixing and water-mass formation in the Australian subantarctic. J Phys Oceanogr 11:1399–1406
Tokinaga H, Xie S-P, Kobashi F, Tanimoto Y (2009a) Local and remote influences of the Kuroshio Extension on the atmosphere. US CLIVAR Var 7:1–4
Tokinaga H, Tanimoto Y, Xie S-P, Sampe T, Tomita H, Ichikawa H (2009b) Ocean frontal effects on the vertical development of clouds over the western North Pacific: in situ and satellite observations. J Clim 22:4241–4260
Tsubouchi T, Suga T, Hanawa K (2007) Three types of South Pacific subtropical mode water: the relation to the large-scale circulation of the South Pacific subtropical gyre and their temporal variability. J Phys Oceanogr 37:2478–2490
Tsubouchi T, Suga T, Hanawa K (2010) Indian Ocean subtropical mode water: its water characteristics and spatial distribution. Ocean Sci 6:41–50
Tsuchiya M (1985) Evidence of a double-cell subtropical gyre in the South Atlantic Ocean. J Mar Res 43:57–65
Uda M, Hasunuma K (1969) The eastward subtropical countercurrent in the western North Pacific Ocean. J Oceanogr Soc Jpn 25:201–210
Vianna ML, Menezes VV (2010) Mean mesoscale global ocean currents from geodetic pre-GOCE MDTs with a synthesis of the North Pacific circulation. J Geophys Res 115:C02016. doi:10.1029/2009JC005494
Wang B, Lin Ho (2002) Rainy season of the Asian–Pacific summer monsoon. J Clim 15:386–398
Welander P (1959) An advective model of ocean thermocline. Tellus 11:309–318
Welander P (1981) Mixed layer and fronts in simple ocean circulation model. J Phys Oceanogr 11:148–152

White WB, Hasunuma K (1982) Quasi-stationary banded structure in the mean zonal geostrophic current regimes of the western North Pacific. J Mar Res 40:1035–1046

White WB, Walker AE (1985) The influence of the Hawaiian Archipelago upon the wind-driven subtropical gyre in the western North Pacific. J Geophys Res 90:7061–7074

White WB, Hasunuma K, Solomon H (1978) Large-scale seasonal, secular variability of the subtropical front in the western North Pacific from 1954 to 1974. J Geophys Res 83:4531–4544

Worthington LV (1959) The 18° water in the Sargasso Sea. Deep Sea Res 5:297–305

Wyrtki K (1975) Fluctuations of the dynamic topography in the Pacific Ocean. J Phys Oceanogr 5:450–459

Xie S-P, Kunitani T, Kubokawa A, Nonaka M, Hosoda S (2000) Interdecadal thermocline variability in the North Pacific for 1958–1997: a GCM simulation. J Phys Oceanogr 30:2798–2813

Xie S-P, Liu WT, Liu Q, Nonaka M (2001) Far-reaching effects of the Hawaiian Islands on the Pacific Ocean–atmosphere system. Science 292:2057–2060

Xie S-P, Deser C, Vecchi GA, Ma J, Teng H, Wittenberg AT (2010) Global warming pattern formation: sea surface temperature and rainfall. J Clim 23:966–986

Xie S-P, Xu L-X, Liu Q, Kobashi F (2011) Dynamical role of mode-water ventilation in decadal variability in the central subtropical gyre of the North Pacific. J Clim 24:1212–1225

Xu L-X, Xie S-P, Liu Q, Kobashi F (2012) Response of the North Pacific subtropical countercurrent and its variability to global warming. J Oceanogr. doi:10.1007/s10872-011-0031-6

Yamanaka G, Ishizaki H, Hirabara M, Ishikawa I (2008) Decadal variability of the subtropical front of the western North Pacific in an eddy-resolving ocean general circulation model. J Geophys Res 113:C12027. doi:10.1029/2008JC005002

Yasuda T, Hanawa K (1997) Decadal changes in the mode waters in the midlatitude North Pacific. J Phys Oceanogr 27:858–870

Yasuda T, Hanawa K (1999) Composite analysis of North Pacific subtropical mode water properties with respect to the strength of the wintertime East Asian monsoon. J Oceanogr 55:531–541

Yoshida K, Kidokoro T (1967a) A subtropical countercurrent in the North Pacific—an eastward flow near the subtropical convergence. J Oceanogr Soc Jpn 23:88–91

Yoshida K, Kidokoro T (1967b) A subtropical countercurrent (II)—a prediction of eastward flows at lower subtropical latitudes. J Oceanogr Soc Jpn 23:231–236

Young RW, Rhines PB (1982) A theory of the wind-driven circulation II. Circulation models and western boundary layers. J Mar Res 40:849–872

Yu Z, Maximenko N, Xie SP, Nonaka M (2003) On the termination of the Hawaiian Lee countercurrent. Geophys Res Lett 30(5):1215. doi:10.1029/2002GL016710

Yuan X, Talley LD (1996) The subarctic frontal zone in the North Pacific: characteristics of frontal structure from climatological data and synoptic surveys. J Geophys Res 101:16491–16508